

605
117

The Structure of a Pacific Narrow Cold Frontal Rainband

David P. Jorgensen¹

NOAA/National Severe Storms Laboratory

Zhaoxia Pu

*Goddard Earth Sciences and Technology Center
University of Maryland, Baltimore County*

Ola Persson

NOAA/Environmental Technology Laboratory

Wei-Kuo Tao

NASA/Goddard Space Flight Center

Submitted to

MONTHLY WEATHER REVIEW

July 26, 2002

¹Corresponding Author Address: David P. Jorgensen, NOAA/NSSL/MARD-Boulder,
Mail Code: N/C/MRD, 325 Broadway, Boulder, CO 80305. E-mail: davej@ncar.ucar.edu

Abstract

A NOAA P-3 instrumented aircraft observed an intense, fast-moving narrow cold frontal rainband as it approached the Pacific Northwest coast on 19 February 2001 during the Pacific Coastal Jets Experiment. Pseudo-dual-Doppler analyses performed on the airborne Doppler radar data while the frontal system was well offshore indicated that a narrow ribbon of very high radar reflectivity convective cores characterized the rainband at low levels with echo tops to ~4-5 km. The NCFR exhibited gaps in its narrow ribbon of high reflectivity, probably as a result of hydrodynamic instability along its advancing cold pool leading edge. In contrast to some earlier studies of cold frontal rainbands, density current theory described well the motion of the overall front. The character of the updraft structure associated with the heavy rainfall at its leading edge varied across the gap regions. The vertical shear of the cross-frontal low-level ambient flow exerted a strong influence on the updraft character, consistent with theoretical arguments developed for squall lines describing the balance of vorticity at the leading edge. In short regions south of the gaps the vertical wind shear was strongest with the updrafts and rain shafts more intense, narrower, and more erect or even downshear tilted. North of the gaps the wind shear weakened with less intense updrafts which tilted upshear with a broader band of rainfall. Simulations using a nonhydrostatic mesoscale nested grid model are used to investigate the gap regions, particularly the balance of cold pool induced to pre-frontal ambient shears at the leading edge. Observations confirm the model results that the updraft character depends on the balance of vorticity at the leading edge. Downshear-tilted updrafts imply that convection south of the gap regions would weaken with time relative to the frontal segments north of the gaps since inflow air would be affected by passage through the heavy rain region before ascent, suggesting a mechanism for gap filling.

1. Introduction

The rainfall patterns within extratropical cyclones are usually organized as mesoscale rainbands (Houze et al. 1976; Rutledge and Hobbs 1984). Of the six main types of rainbands classified by Hobbs (1978), the most intense rainfall rates are usually associated with Narrow Cold Frontal Rainbands (NCFRs), a few kilometers wide and usually found close to the position of the surface cold front. Studies of NCFRs with Doppler radars have shown that they are associated with strong but relatively shallow updrafts of up to 20 m s^{-1} (Carbone 1982; Hobbs and Persson 1982; Parsons 1992) near the leading edge of the surface front. The strong updrafts occurred in the absence of appreciable potential instability. The radar echo tops are often seen to be 4-5 km AGL. The convective cells within the NCFR are often severe (heavy rain, hail, strong surface winds, etc), in spite of their shallow nature, and sometimes exhibit gravity current-like structures and motion (Braun et al. 1997; Carbone 1982; Parsons et al. 1987; Koch and Kocin 1991). In fact, the NCFR studied here produced hail along the California coast at landfall, and was particularly hard to detect by coastal radars due to its shallowness. Rather than being strictly two-dimensional and continuous, however, the NCFR has often been observed to exhibit breaks or gaps in the horizontal radar reflectivity depiction (James and Browning 1979; Hobbs and Biswas 1979). Usually, the precipitation cores are observed to be oriented at a slight angle with respect to the orientation of the synoptic cold front (Hobbs and Persson 1982; Wakimoto and Bosart 2000). The gap regions of some NCFRs have been observed to be of various sizes (James and Browning 1979). Locatelli et al. (1995) termed gaps greater than 10-12 km as “large” gaps and suggested that they may be dynamically different from smaller gaps. Wakimoto and Bosart (2000) provided fine scale kinematic observations of these large gaps using airborne Doppler radar. Although the Wakimoto and Bosart (2000) case had relatively weak rainfall (maximum

radar reflectivity within the band was ~30 dBZ) compared with other case studies, including this one with maximum reflectivities ~55-60 dBZ, their analysis clearly showed that the gap regions were areas devoid of strong updrafts and associated with weak surface wind discontinuities. The maximum core reflectivity could be displaced downwind from the core updraft and could be collocated with the weakest surface discontinuity, a refinement to earlier NCFR analysis by Hobbs and Persson (1982).

Horizontal shearing instabilities (Haurwitz 1949) along the leading edge of the advancing cold front has been often advanced as the mechanism of the gap structure, although other mechanisms, such as a trapped gravity wave (Brown et al. 1999) or perhaps differential advection of precipitation particles by the core-relative winds could define the NCFR structure (Locatelli et al. 1995).

Two-dimensional cross-frontal sections through the leading edges of NCFRs often reveal a gravity current-like structure (Koch and Kocin 1991; Chen et al. 1997). The gravity current, fed by low-level cold air advection and evaporative cooling from intense precipitation along the leading edge of the NCFR, helps maintain the NCFR updraft through the balance of the solenoidally forced vorticity within the gravity current and the vorticity produced by strong vertical wind shear associated with the environment, specifically the low-level jet ahead of the NCFR (Rotunno et al. 1988). High-resolution mesoscale numerical simulations (Chen et al. 1997) of NCFRs have replicated many of the structural features of NCFRs, including the low level gravity current, but limitations in the model's cloud microphysical parameterization and grid resolution may have precluded using the model to test the hypothesis that evaporative cooling was important in maintaining the gravity current and associated frontal contraction and NCFR structure (Koch 1999).

This study describes pseudo-dual-Doppler radar data, flight level in-situ data, and dropsonde measurements from a National Oceanic and Atmospheric Administration (NOAA) instrumented WP-3D aircraft in the northwest Pacific during the *Pacific Landfalling Jets Experiment* in January-February 2001 (PACJET-2001). The overarching goal of PACJET is to develop and test methods to improve short-term (0-24 h) forecasts of damaging weather on the U. S. West Coast in landfalling winter storms emerging from the data sparse Pacific Ocean. Specifically, PACJET provides the data sets with which to improve understanding of landfalling storms, as well as providing unique data to forecasters for real-time². In this paper we present analyses of an NCFR observed by the P-3 on 19 February 2001. We further supplement the Doppler analyses with numerical mesoscale model results using the Penn State-NCAR MM5 to explore the relationships between low-level processes and the gap regions of the NCFR.

2. Aircraft Data and Analysis Approach

The primary observational platform used in this study is the NOAA P-3 aircraft with its vertically scanning X-band Doppler radar (Jorgensen et al 1983). The P-3 was deployed from its PACJET base of operations in Monterey California. In addition to its Doppler radar and wide variety of in-situ sensors, the NOAA P-3 is also equipped with a horizontally scanning lower fuselage C-band radar for mapping of radar reflectivity to a range of about 400 km from the aircraft. The various parameters of the P-3 radars are shown in Table 1.

The NOAA P-3 airborne Doppler radar (Fig. 1) is an X-band, vertically scanning radar mounted in the tail section of the P-3 that uses the fore/aft scanning technique (FAST, Jorgensen et al. 1996) to alternatively scan the antenna fore and aft by about 20° from a plane perpendicular

² For more information on PACJET see the web site:
<http://www.etl.noaa.gov/programs/2002/pacjet/>.

to the flight track during a period of two full antenna rotations. As the aircraft flies a relatively straight flight path, the antenna sweeps out a three-dimensional volume with the fore and aft beams intersecting at approximately 40° angles. The horizontal velocity is estimated from these two estimates in the vertical region defined by $\pm 45^\circ$ elevation angle. Restricting the elevation angle to $\pm 45^\circ$ minimized the deleterious effects of uncertainties in terminal fallspeed on the horizontal wind estimate.

The radar uses a batch-mode “staggered pulse-repetition frequency (PRF)” approach to extend the unambiguous radial (Nyquist) velocity using two PRFs (Jorgensen et al. 2000). The two PRFs used in this study were 3200 and 2133 s^{-1} , which produced an extended Nyquist interval of 51.4 $m s^{-1}$; hence there were few “folds” in the radar data that had to be manually corrected. The few processor dealiasing mistakes ($\sim 3\%$ of the total gates) were removed using the NCAR SOLO radar editing software package. Following editing, three-dimensional winds were constructed using the pseudo-dual-Doppler methodology described in Jorgensen et al. (1996). The Doppler data from 19 February was collected with the antenna in sector scanning mode so the horizontal data spacing was ~ 700 m. The Doppler data was interpolated to Cartesian grids with a spacing $\Delta x = \Delta y = 0.7$ km and $\Delta z = 0.5$ km. The vertical grid levels were constructed relative to mean sea level (MSL). Vertical velocity is estimated from vertical integration of horizontal divergence estimates. The integration is from the top of the echo (where $w=0$ is assumed) to the surface. An O’Brien (1970) divergence correction is made to the vertical column to insure that $w=0$ at the ground. A two-step Leise filter (Leise 1981) was applied to the velocity data prior to computation of the vertical velocity to remove artifacts of wavelength less than about $4\Delta x$ and retain greater than 90% of the energy of features with wavelength $> 8\Delta x$.

The maximum range of the radar is about 45 km, which represents a maximum time displacement between fore and aft scans of about 4 minutes. During that time, as well as for the duration of each flight leg that comprises the complete volume scan, the weather within the analysis domain is assumed to be “stationary”. Stationary over the 8-10 minutes, required to complete the volume scan, is a fairly common assumption for airborne and ground-based Doppler radar studies. Nevertheless this assumption is a limiting factor in interpreting the data collected on relatively fast evolving systems, like individual convective storm cells.

To determine NCFR motion a sequence of lower fuselage radar composites were examined over about a 6-hour period to determine motion of the leading edge. Various “gaps” or “kinks” in the NCFR could be reliably tracked for several hours and their displacements aided in the determination of overall NCFR motion. The NCFR studied here was moving relatively rapidly: toward 053° at 18 m s^{-1} over the approximately 6 hour duration of the P-3 investigation. The analysis grid is moved to compensate for this system motion, and wind vectors displayed are relative to the moving system. At various times during the flight individual convective cores or pieces of the NCFR could be seen moving slightly differently that this mean NCFR motion, usually slightly faster or slower by an average of about $\pm 15\%$ of direction and $\pm 2 \text{ m s}^{-1}$. We evaluated the effect of using this *core-relative* motion, rather than the mean NCFR motion, for one flight leg segment where the difference between the two motions was the greatest: about 20% in direction and 5 m s^{-1} in speed. The differences in the pseudo-dual-Doppler wind analyses and computed fields like vertical velocity was slight. Rather than compute separate core-relative motions for each flight leg segment, as was done by Braun et al. (1997) in their study of an offshore NCFR in 1993 using the same P-3, we chose to utilize the mean motion to facilitate comparisons between different time periods.

The radar reflectivity field was determined by taking the maximum of either the fore or aft scans at each Cartesian point. Precipitation fall speeds were subtracted from the radial wind estimates and were estimated by two empirical relationships between terminal fall speed and radar reflectivity: one for rain (Joss and Waldvogel 1970) applied below 2.25 km MSL and one for snow (Atlas et al. 1973) applied above 2.75 km MSL. Between 2.25 km and 2.75 km the terminal fall speed is determined as a weighted sum of the snow and rain relationships.

3. Overall NCFR structure from aircraft observations

The P-3 departed Monterey at 0134 UTC and arrived at the vicinity of the NCFR at about 0320 UTC. The 19 February NCFR was intercepted by the P-3 approximately 560 km offshore from its base at Monterey, California over the eastern North Pacific Ocean. The P-3 monitored the NCFR, using a variety of Doppler legs, ascent/descent soundings, and low-level flux stacks until returning to Monterey at 0940 UTC, just ahead of the heavy rainfall of the NCFR at landfall.

a. NCFR environment

Fig. 2 shows the 0000 UTC 19 February 2001 500 hPa analyses from NOAA's National Centers for Environmental Prediction (NCEP). Fig. 3 shows the surface analysis, and Fig. 4 shows an infrared satellite image at 0400 UTC about the aircraft had begun its Doppler flight pattern investigation. The advancing cold front marked the surface position of the NCFR, which was situated just ahead of a 500 kPa deep occluded low to the northwest, with a strong westerly jet at 500 kPa of about 25 m s^{-1} to the west of the surface frontal position. Westerly to west-southwest winds were observed by ships to the west of the front. At landfall near the San Francisco Bay area and southward, the frontal system produced heavy rain and surf along the coast, and a funnel cloud report near Sacramento, California.

The NCFR existed in an environment virtually devoid of instability yet possessing high low-level shear. A sounding constructed by compositing a dropsonde deployed by the P-3 at 0234 UTC (below 500 hPa) with the 0000 UTC radiosonde launched at Oakland, California (data above 500 hPa) is shown in Fig. 5. The dropsonde was deployed as the P-3 approached the NCFR in the warm sector about 150 km from the NCFR. The convective available potential energy (CAPE) was only $\sim 50 \text{ J kg}^{-1}$, yet the surface winds were southerly at about 15 m s^{-1} , turning to southwesterly at near 25 m s^{-1} by 700 hPa. Such low instability/high shear soundings are characteristic of NCFR environments (Houze et al. 1976).

b. Precipitation structure

The P-3s lower fuselage radar (LF) composite over a 34-minute period indicates the extensive horizontal extent of the two bands (Fig. 6). The horizontal extent of the NCFR was quite extensive with a ribbon of high near surface reflectivity extending over 200-300 km in length with extensive cloud cover downstream and lighter precipitation ahead (to the east) and behind (to the west) of the surface frontal position. Maximum reflectivity of the core cells often exceeded 55 dBZ. The narrow ribbon of 40 dBZ reflectivity indicating the position of the NCFR was often not continuous, but broken by periodic “gap regions” (or “kinks”) of lighter reflectivity indicating breaks in the NCFR with a spacing between the gaps of 50-75 km. Hobbs and Persson (1982) and Wakimoto and Bosart (2000) also noted the discontinuous nature of NCFRs.

In contrast to the Wakimoto and Bosart (2000) finding that there was about a 20° clockwise angle of rotation between the cold frontal position and the long axis of the precipitation cores making up the line in their case study, this NCFR did not have any difference in the orientation or motion of the cores between the gaps and the overall frontal motion. Although there were

times when individual cores did move faster than the line as a whole, leading to the “bow-shaped” regions of the NCFR and breaks north and south of it, the convective line was constantly reforming and individual precipitation cores could not be consistently tracked as entities within the narrow ribbon of high reflectivity to yield a separate core motion.

c. Environmental soundings

A total of 9 aircraft sounding profiles were obtained during the P-3 flight. Eight profiles were obtained ahead of the convective line and one behind. Of the 8 ahead profiles, 2 have a height range from 300 m - 5500 m and the other 6 have a height range of 150 m - 1600 m. The post-frontal profile had a range of 300m-5500m. In a front-relative sense, they are spaced 20-200 km ahead of and behind the front and at various locations along the front. Figure 5 shows the profiles with the 300 m - 5500 m height range, of which two are ahead (denoted “Pre-frontal (N)” and “Pre-Frontal (S)” on the LF radar plot of Fig. 6) of the line and one is behind (marked “Post-Frontal”). Of the two taken ahead of the NCFR, the “Pre-frontal (S)” was obtained 200 km further south than the “Pre-frontal (N)”. The post-frontal profile had a north-south position roughly between the two prefrontal profiles. Since the NCFR had nearly a north-south orientation at the time of the investigation, the u and v wind profiles indicate wind components perpendicular to and along the NCFR, respectively. Examination of these profiles indicates differences in both the cross-frontal and along-frontal directions. Far from being embedded in a homogeneous environment, the NCFR had substantial differences in the north-south direction. For instance, the along frontal low-level jet (LLJ) is strongest near the center of the NCFR (in the u component or along-front direction), reaching 32 m s^{-1} . In the two prefrontal profiles shown, the LLJ has a velocity of 24-29 m s^{-1} . It is lower in altitude to the south (about 500 m) and higher to the north (1100 m). The air ahead of the convective line is potentially unstable

$((\partial(\theta_e)/\partial z < 0)$ up to 3-4 km, where θ_e is the equivalent potential temperature, with the potential instability greater to the south ($\partial(\theta_e)/\partial z = -9\text{K}/3000\text{m}$) than to the north ($\partial(\theta_e)/\partial z = -2\text{K}/3500\text{m}$). However, the prefrontal air is statically stable ($((\partial(\theta_v)/\partial z > 0)$, even near the surface. Note, however, that the prefrontal air is substantially cooler to the north than to the south, and that the mid-level winds are stronger to the south. Finally, the wind direction backs by 25-30 degrees from the south to the north, consistent with the bow shape of the convective line and the front. Behind the front, the air is cooler and drier at all levels. Except above 500 mb, the wind speed is also 7-10 m/s weaker than ahead of the front, and the wind direction has veered, consistent with the passage of a cold front. The post-frontal air is potentially unstable to about 2 km, and is statically neutral in the lowest 500 m. The presence of small convective clouds in the post-frontal air seen by on-board observers as well as on the satellite picture (Fig. 4) is evidence of this low-level post frontal instability.

c. Kinematic and precipitation structure

Fig. 8 shows the reflectivity and Doppler wind structure of the NCFR in the domain labeled “A” in Fig. 6 at 1.0 km MSL and slightly higher at 1.75 km MSL (Fig. 9). At the time of observation the NCFR was oriented approximately north-south with several distinct “bows” in the line toward the east. Three such NCFR gaps in Fig. 8 are seen at approximate locations of $y=16$ km, $y=50$ km, and $y=100$ km. Weaknesses in the radar horizontal radar reflectivity, and even complete breaks in the narrow ribbon of high reflectivity, are seen at those locations. The apex of each bow was associated with an enhancement of low-level radar reflectivity and a larger component of westerly rear inflow behind the line. Slightly aloft (Fig. 9) the flow behind the line reverses from westerly to southerlies or even easterly, depending on location relative to the gaps in the line. In general the gap regions and regions just north of the gaps, are locations of

enhanced front to rear flow at 1.75 km MSL, while the bow regions are locations of strongest rear to front flow at 1.00 km MSL. The line structure for the region “B” in Fig. 6 is shown in Fig. 10 for 1.00 km MSL and Fig. 11 for 1.75 km MSL. A bow in the NCFR is seen at approximately $y=29$ km with a gap just south and north of it. An enhanced front to rear flow on each side of the bow apex is also seen.

Earlier studies have hypothesized that the breaks in the NCFR were due to horizontal shearing instabilities of the along-front wind (Wakimoto and Bosart 2000; Carbone 1982; Braun et al. 1997). Linear wave theory (Haurwitz 1949) would predict that the fastest growing mode would be ~ 7.5 times the width of the shear zone across the leading edge of the front. To access this possibility, individual tail radar sweeps were examined during the along frontal flight segment from 0520-0554 UTC (over 300 sweeps). The radial velocity for each sweep was examined to identify the transition at low-levels from receding to approaching radial velocity, indicating the shear zone at the leading edge of the NCFR. The average shear zone width was determined to be ~ 2.97 km with a standard deviation of ~ 0.465 km. A correction was applied to account for the fact that the beam did not cut the NCFR perpendicularly, but rather at an angle $\sim 20^\circ$ from perpendicularity because of the fore/aft scanning technique. The range of shear zone width, 2.40-3.55 km implies, according to the linear wave theory, that the most unstable wavelength is ~ 18.0 - 26.6 km. This wavelength is a reasonable approximation to the gap distances revealed in the LF imagery in Fig. 6, providing evidence that perhaps shearing instability was a mechanism responsible for the gap structure of this NCFR.

The vertical cross-line structure is best seen in vertical cross sections (Fig. 12) on each side of a “gap” or break in the NCFR (at about $y=50$ km) taken perpendicular to the orientation of the NCFR. In both cross sections, low-level convergence was generated from the south-southeasterly

flow ahead of the NCFR with the post-frontal westerly flow behind it. This low level convergence supported the strong updrafts in the NCFR convective cores. The echo tops were only 4-4.5 km MSL, about half of the heights typical in midwest U.S. convective storms. Because of the relative shallowness of this NCFR, coastal National Weather Service (NWS) radars did not depict it very well (not shown here) due to beam overshooting. The cross section shows updrafts along the leading edge to be ~5-10 m/s. An overshooting top along with strong rear to front flow below about 1.8 km MSL was also seen. The strong temperature discontinuity is indicated by the descent in the bright band height from around 1.8 km MSL to the east of the NCFR to about 1 km MSL behind it. The stronger front to rear flow in the northernmost cross section A-A' (Fig. 12a) is clearly seen, along with the near surface convergence being located near the eastern edge of the high reflectivity region. The precipitation core along with the principal updraft is primarily vertically erect below about 1.8 km and slightly rearward sloping about that level. In contrast, the cross section south of the gap (Fig. 12b) shows the strongest near surface convergence to be near the western, or rearward, edge of the high reflectivity core with an indication of a forward leaning precipitation core. This configuration of updraft sloping downshear leads to rain falling into the inflow air prior to rising in the updraft, a situation that would eventually lead to weakening of the convection by weakening the instability.

d. Vertical circulations at the leading edge of the NCFR

The different structural nature of the NCFR revealed in the two cross-sections in Fig. 13 indicates that different physical processes are acting on the NCFR across the gap regions. Many previous studies have stressed the importance of gravity current dynamics, particularly frictional processes within the boundary layer, to the character of the lifting along the leading edge of the surface front (Chen et al. 1997). Individual scans of the P-3s tail radar Doppler radial velocity

from this NCFR clearly show gravity current-like structure (not shown) as the “nose” of the leading edge of the cold pool marks the edge of the advancing cold air. Other examples of radar scans through NCFR leading edges can be seen in Wakimoto and Bosart (2000). Parsons (1992) showed that low-level cross-frontal ambient wind shear determines the character of the lifting at the cold pool leading edge. Using a series of numerical experiments he demonstrated that an “optimal” vertical shear balance exists where the frontal updraft is upright and sustained. Rotunno et al. (1988) offers a complementary viewpoint of this process involving horizontal vorticity balance between the low-level environmental wind shear and the vorticity produced by the cold pool (RKW theory). A sustained, erect updraft is produced when the vorticity produced at the leading edge of the cold pool is balanced by the advection of vorticity from the ambient environment. Weisman (1993) extended the Rotunno et al. (1993) ideas to bow-echo systems that produced strong rear-inflow using a series of numerical simulations. In a two-dimensional framework (Fig. 13) the tilt of the principal updraft of a convective system can be downshear (Fig. 13a) if the cold pool generated vorticity is less than the ambient environmental shear, or upright (Fig. 13b) if the two opposing shears are roughly in balance, or even upshear (Fig. 13) if the cold pool generated vorticity dominates over the environmental shear. Weisman (1993) termed the sequence as “evolutionary” since the strengthening and deepening of the cold pool takes place over a finite time and in his simulations the bow-echo evolved into a mature system once the cold pool became developed. Once the system tilts upshear, a rear-inflow is generated in response to the buoyant updraft air being lifted over the cold pool by the establishment of a hydrostatically generated mesolow just behind the leading edge (Jorgensen et al. 1997). Such a strong upshear tilt would not lead to intense precipitation along a narrow zone near the surface

frontal position, but a broad zone of precipitation extending to the rear of the system (Parsons 1992).

Earlier work by Parsons (1992), who studied NCFR structure with a two-dimensional version of the Klemp and Wilhelmson (1978) cloud model, emphasized the importance of cross frontal vertical shear in determining the character of the frontal updraft. In this earlier treatment the NCFR was treated as a two-dimensional entity. Clearly, this NCFR is not a strictly two-dimensional. However, we hypothesize that the same RKW theory can be applied to NCFR structure that involves breaks and gaps in the line if the vorticity balance is considered to be local to a given bow-shaped element. Brown et al. (1999) argues that density current theory should only apply in local regions of the cold front, especially near precipitation cores. Wakimoto and Bosart (2000) found that their NCFR density current arguments could not explain the observed motion of the overall front, but did describe the motion of precipitation core segments of the NCFR. To evaluate if gravity current theory approximates the front's overall motion we evaluate the expression for propagation speed of a density current, retarded by opposing prefrontal flow, by Simpson and Britter (1980):

$$c = k \sqrt{gh \frac{\Delta \bar{\theta}_v}{\bar{\theta}_{vc}}} + bu_0 \quad (1)$$

where c is the frontal propagation speed, g the gravitational acceleration, h is the depth of the cold pool, u_0 is the prefrontal cross-front wind component (negative for a wind toward the front), $\Delta \bar{\theta}_v$ the mean difference in virtual potential temperature across the front, $\bar{\theta}_{vc}$ the mean virtual potential temperature in the cold air, k the internal Froude number (0.7-1.1 Koch 1984), and b is a constant equal to 0.6.

The calculation of c is based on the aircraft's post-frontal decent sounding (the location is shown in Fig. 6, the sounding values in Fig. 7). For this sounding $\Delta\bar{\theta}_v = 2.1$ K, $\bar{\theta}_{vc} = 300.1$ K, and $h = 2.1$ km. The Doppler winds indicated u_0 was ~ 7.1 m s⁻¹ averaged over a 3 km by 15 km region ahead of the front and averaged over a depth corresponding to the cold pool. Using Eq. (1) the frontal speed was computed to be ~ 15.5 - 20.3 m s⁻¹, depending on the range of the Froude number. The observed speed of the overall front was 18 m s⁻¹, thus the gravity current velocity reasonably approximated the front's observed motion. We note, however, that many previous studies have found that gravity current theory does not properly describe NCFR motion. In particular, Wakimoto and Bosart (2000) showed that while the overall frontal motion was not described by gravity current theory, individual precipitation core segments that had different orientations and motions than the overall front, was well described by the theory. Significant long lasting individual precipitation cores, like those described by Wakimoto and Bosart (2000) were not observed in this NCFR. The horizontal pseudo-dual-Doppler wind plots shown in Fig. 8-10, however, show the NCFR was not a two-dimensional feature. Moreover, the descent sounding was ~ 200 km to the rear of the leading edge and nearly 45 minutes after the time of the dual-Doppler analysis presented in Fig. 8-10, so the validity of the calculation of density current speed to specific local regions of the NCFR is questionable. The cross sections on each side of the NCFR gap (Fig. 12) show the depth of the rear inflow (and probably the depth of the cold pool) to be approximately the same, and the depth and strength of the inflow wind shear to be similar. The strength of the cold pool across the NCFR gap, however, cannot be accurately determined from the Doppler radar data so it is difficult to assess the validity of density current theory locally.

Similar to the density current evaluation, the balance of vorticity argument presented by RKW can be evaluated by comparing the horizontal vorticity induced by the density changes across the leading edge of the cold pool (the parameter C in Fig. 13). That parameter can be estimated by

$$C = \sqrt{gh \frac{\Delta \bar{\theta}_v}{\bar{\theta}_{vc}}} \quad (2)$$

Evaluating Eq. (2) using the post-frontal sounding data gives $C \sim 12 \text{ m s}^{-1}$. The pre-frontal ambient shear-induced vorticity can be represented by Δu , which is the vertical shear over the depth of the cold pool (h) and can be readily estimated from the pseudo-dual-Doppler derived winds. Two mean profiles of cross-frontal winds are shown in Fig. 14, taken over a 5 km by 10 km box ahead of the NCFR centered on the western end point of the two cross sections A-A' and B-B' (shown in Fig. 12). The plot shows stronger low-level pre-frontal shear (i.e., Δu over the lowest 1.8 km) for the profile B-B' south of the gap ($\Delta u \sim 15 \text{ m s}^{-1}$), than the profile near A-A' north of the gap ($\sim 4 \text{ m s}^{-1}$). The pre-frontal Δu south of the gap is slightly larger than the horizontal vorticity shear due to the cold pool computed by Eq. (2), which Rotunno et al. (1988) hypothesized would lead to an “sub-optimal” condition in which convection at the leading edge of the cold pool is downshear tilted (Fig. 13a). Conditions north of the gap are such that $C > \Delta u$ and RKW ideas would predict an upshear-tilted updraft with a broader rainfall maximum, in agreement with the radar cross section (Fig. 12a).

To examine the character of the updraft flow around other gaps in the NCFR many cross sections were examined. A summary of the survey is shown in Fig. 15, which shows the relationship of the updraft core locations to the rainfall maxima and 0.5 km AGL relative wind. The regions where the updraft cores, very nearly coincident with the near surface convergence

maxima, coincided with maximum reflectivity are labeled “erect” for the vertically erect nature of the reflectivity core on cross sections. Similarly, where the updraft core is east (west) of the reflectivity maxima the region is labeled “upshear” (“downshear”), respectively. The repeatable nature of the relationship of updraft tilt around the NCFR gaps is seen. Regions north of gaps are characterized by erect updrafts then transitioning to upshear then downshear tilted updrafts. Profiles of cross frontal winds in each of the regions labeled “erect”, “upshear”, and “downshear” (not shown) confirm the relationship shown in Fig. 14, i.e., in upshear tilted regions the pre-frontal low-level shear is much weaker than the value of C computed by Eq. (2).

Other factors, such as spatial and temporal variations of C due to diabatic cooling in the cold air due to hydrometeor evaporation and melting or boundary layer modification of the cold pool due to sea-air flux and possible generation of horizontal vorticity by horizontal buoyancy gradients not associated with the leading edge of the cold pool (Lafore and Moncrieff (1989), represent possible limitations to the application of RWK ideas in explaining NCFR behavior. Nonetheless, the coevolving fields of wind and NCFR precipitation structure are highly suggestive of the relevance of RKW theory in explaining this NCFRs structure. Also, some of the other factors that limit the application of RKW theory to deep convective lines are mitigated here. For example, although Weisman (1990) found that certain squall line environments contained other sources of vorticity, other than the balance at the leading edge, which need to be considered when assessing the behavior of leading edge updrafts, in our NCFR case the limited potential instability and small buoyancy gradients limit those concerns. Yu and Smull (2000) performed similar calculations of vorticity balance using buoy and airborne Doppler observations for an NCFR approaching the Northern California coast and found that, in the mean, density current theory did adequately describe the motion of their NCFR. Moreover, the

vertical shear in advance of the front was generally “suboptimal” (i.e., $C \gg \Delta u$) until right before landfall consistent with vertical cross sections that showed frontal updrafts sloping over the cold air and upshear tilt. They also noted a progression toward more erect updrafts, and narrower rainfall patterns, as the NCFR moved closer to the coast coincident with increases in prefrontal low-level shear. They concluded that low-level upstream blocking was an important factor in changing the character of the frontal updraft as the front made landfall, a factor not affecting our NCFR.

4. Numerical model simulations

Since in-situ observations of cold pool strength and depth in the cold air across the NCFR gap regions was not available in sufficient detail for the 19 February flights, we utilize mesoscale numerical model simulations to assess the role of vorticity balance at the NCFRs leading edge in defining the character of the frontal updrafts.

a. Model description

The nonhydrostatic version of the Penn-State-NCAR MM5 (Dudhia 1993) uses observed meteorological analyses as an initial condition for time-evolving simulations of the NCFR. The model uses a nested grid structure to simulate cloud processes on grids of xx km, 4 km, and 1.3 km. The model was initiated from the NOAA/National Centers for Environmental Prediction (NCEP) archived “ETA” model analyses at 1200 UTC 18 February 2001 and allowed to run for 18 hours. The “valid time” for comparison to the P-3 observations is therefore 0600 UTC 19 February 2001. No ad hoc initialization using a traditional cold pool or warm thermal bubble was used, rather the clouds generated in the simulations were the result of explicitly resolved mesoscale convergence fields. The principal physical processes involved:

1. An explicit cloud microphysical scheme that contains water vapor, cloud water, and rainwater when the air temperature is above 0°C; below 0°C the cloud water and rainwater are treated as cloud ice and snow.
2. A cumulus parameterization scheme (Grell 1993) on all but the 1.3 km grid.
3. A high resolution planetary boundary layer scheme (Zhang and Anthes 1982).

b. Model results

A plan view of the 850 hPa system relative flow and precipitation from the 4 km grid mesh of the modeled NCFR after 17 hours of integration is shown in Fig. 16. The model produced an arc-shaped rainband that was moving $(u,v) = (12.8, 15.4) \text{ m s}^{-1}$ with the apex of the bow near 34.5N. Much like the observed NCFR, the modeled version was near the bottom of the large-scale trough. Model simulated precipitation for the 5 hour time period 13-18 hours after model initialization (which corresponds to 0100-0600 UTC 19 February 2001) is shown in Fig. 17. During this 5-hour period, the simulated NCFR was bow-shaped and propagated rapidly eastward much like the observed motion of the NCFR. Near the apex of the NCFR bow, its motion was reasonably similar to the observed NCFR motion from LF image sequence of $(u,v) = (14.4, 10.8) \text{ m s}^{-1}$. Rather than being a continuous ribbon of rainfall, however, as the P-3 LF radar indicated between 33N-36N (Fig. 6), the simulated NCFR exhibited gaps, particularly near 35N, with precipitation cores moving as discrete elements. The motion of these cores was not uniform along the NCFR. North of about 36N the cores moved mostly northerly, while south of about 32N the core motion was east-northeasterly, probably in response to the flow pivoting around the synoptic surface low shown in the satellite photograph near 39N, 134W at this time (Fig. 4). The more discrete nature of the precipitation cores resembled the NCFR studied by Wakimoto and Bosart (2000).

The modeled NCFR structure around the gap region near 35N is revealed in the surface precipitation and surface equivalent potential temperature (θ_e) analyses for 0600 UTC 19 February 2001 (Fig. 18). South of the gap region the coldest surface θ_e was along the leading edge of the precipitation in a narrow ribbon. Minimum θ_e within the ribbon associated with the strongest surface precipitation was ~ 296 K, a deficit of ~ 12 K from the surface values east of the leading edge of ~ 308 K. North of the gap region the θ_e deficit was ~ 8 K, but rather than concentrated in a narrow ribbon the leading edge was more diffuse and extended rearward farther than the deficit south of the NCFR gap.

To evaluate the vorticity balance at the NCFR leading edge, the inner model domain (shown in Fig. 18) was divided into eight regions, four behind the line and four in front of the line. Each domain was 0.5° of latitude by 0.6° of longitude in area with four of the domains to the north of the gap (domains labeled “B1 and B5” and “B2 and B6”), and four to the south (domains “B3 and B7” and “B4 and B8”). Mean vertical profiles of u (east-west or cross-frontal wind, m s^{-1}), v (north-south or along-frontal wind, m s^{-1}), w (vertical velocity, m s^{-1}), and potential temperature (K) are plotted in Fig. 19. Fig. 19a, the mean profile of cross-frontal wind in each of the domains, shows that the low-level cross-frontal wind shear ahead of the front and over the depth of the cold pool, 1.8 km, increases from north to south (B5 through B8). This behavior was also seen in the P-3 aircraft ascent/descent soundings (Fig. 20) taken about 100 km north and south of the apex of the NCFR that was located near 35 N. This change in pre-frontal shear implies that if the circulation due to the cold pool were relatively constant, the character of the frontal updraft would vary from an upshear tilted broad precipitation zone to the north (i.e., $C > \Delta u$; Fig. 13c) to a frontal zone to the south that is either upright ($C \sim \Delta u$; Fig. 13b) and narrow or downshear tilted ($C \ll \Delta u$; Fig. 13a). To the extent that the average wind profiles in B2-B6 and B3-B7 represent

conditions at the leading edge of the NCFR, the RKW balance arguments applied to the model results are consistent with the P-3 observations across the gap. That is, Δu in the lowest 1.8 km goes from $\sim 6 \text{ m s}^{-1}$ in B6 (north of the gap) to over $\sim 8 \text{ m s}^{-1}$ in B7 (south of the gap). The along-front wind component (Fig. 19b) shows that the pre-frontal low-level jet is also stronger to the south. The post-frontal regions are dominated by subsidence below about 3 km (Fig. 19c) and rising motion above. The potential temperature profiles (Fig. 19d) show about a 2 K decrease across the leading edge with the strongest decreases to the north. Above the cold pool ($\sim 1.8 \text{ km}$) the mean profiles of potential temperature are nearly identical.

The model simulation was similar to the P-3 observations in a number of respects. A model east-west cross section north of the break along 35.5N is shown in Fig. 20. A rearward tilted updraft, in agreement with RKW theory, is seen. Model computed radar reflectivity extended only to $\sim 4.5 \text{ km}$, in agreement with the observations, with the maximum low-level reflectivity to $\sim 45 \text{ dBZ}$. Some evidence of weak convective scale downdrafts at the low levels of heavy rain areas are seen.

5. Summary and conclusions

P-3 radar, dropsonde, in-situ data, and numerical MM5 simulations have been used to document the precipitation and kinematic structure of a strong NCFR well offshore of the U.S. Pacific Northwest. Many aspects of this NCFR structure have been seen in previous studies, including 1) gaps or breaks in the NCFR's narrow precipitation zone at the leading edge, perhaps due to horizontal shearing instability; 2) a strong frontal updraft at the leading edge of the advancing cold pool in spite of the absence of potential instability; 3) strong ambient environmental low-level shear of the inflowing air; 4) low-level jet reaching a peak near 1.5 km AGL ahead of the NCFR and flowing roughly parallel to it; and 5) a "rear-inflow" jet of westerly

air behind the front peaking at near 1 km AGL. Other principal NCFR features documented in this study are:

A consistent variation of updraft tilt on either side of the NCFR breaks. On the south side of the gap the NCFR is bowed to the east with the strongest near surface convergence on the western side of the rainfall maximum. The inflowing air thus flows through the heavy precipitation before rising and tilting downshear. To the north of the gap the updraft is erect then transitions to an upshear tilt.

Associated with the changes in frontal updraft character are changes in the pre-frontal cross-frontal low-level wind shear. In regions of downshear tilt there is strengthening of the shear, with upshear tilt there is a weakening of the shear, consistent with RKW theory.

There was very little difference in the strength of the cold pool across the gap regions well behind the leading edge.

The findings presented here suggest that the mechanism for gap maintenance is not self-sustaining. Once the gap forms (due to hydrodynamic instability or some other mechanism) the convection along bow shaped segment to the south of the gap would eventually weaken with time, relative to the erect or upshear tilted convection north of the gap, since the inflow sustaining the updraft would flow *through* the heavy rainfall. Rain induced cooling of the inflow air would reduce whatever small amount of instability exists in the environment. That the gaps existed for such a long period in the simulation is probably a testament to the near saturated condition of the inflow. P-3 radar observations of this NCFR suggest that the gaps did not

persist over several hours. Older gaps filled and newer ones developed over the 5 hours period of investigation.

This study, along with the studies of Braun et al. (1997) and Yu and Smull (2000), and Wakimoto and Bosart (2000), have shown the utility of using instrumented aircraft to investigate the three-dimensional mesoscale structure and behavior of frontal rainbands. Future aircraft investigations of NCFRs should address the evolution of NCFR breaks by focusing on repeated passes around a single break (perhaps using “box” patterns) for several hours. The more continuous data would allow monitoring of the strength of the cold pool behind the gap and convective core regions and allowing hypotheses to be generated concerning the mechanisms responsible for gap filling.

Acknowledgments. We wish to acknowledge the efforts of the NOAA P-3 flight crews from the Aircraft Operations Center in Tampa, FL who executed the flight patterns used in this study, particularly the flight director, Tom Shepherd, and the radar engineer, James Barr. Without the dedication and enthusiastic support of the AOC crew for our scientific endeavors the collection of airborne Doppler radar data near hazardous weather conditions would not be possible. Robert Hueftle was instrumental in development of the Doppler wind synthesis and display software. Editing of the radar data was accomplished with the NCAR/SOLO software package provided by Dick Oye of NCAR/ATD. We are grateful to Morris Weisman of NCAR for providing Fig. 13.

References

- Atlas, D., R. C. Srivastava, and R. S. Sekhon, 1973: Doppler radar characteristics of precipitation at vertical incidence. *Rev. Geophys. Space Phys.*, **11**, 1–35.
- Barnes, G. M., and K. Sieckman, 1984: The environment of fast- and slow-moving tropical mesoscale convective cloud lines. *Mon. Wea. Rev.* **112**, 1782–1794.
- Biggerstaff, M. I., R. A. Houze, Jr., 1991: Kinematic and precipitation structure of the 10–11 June 1985 squall line. *Mon. Wea. Rev.*, **119**, 3034–3065.
- Braun, S. A., R. A. Houze, Jr., B. F. Smull, 1997: Airborne dual-Doppler observations of an intense frontal system approaching the Pacific Northwest coast. *Mon. Wea. Rev.*, **125**, 3131–3156.
- Brown, S. A., J. D. Locatelli, and P. V. Hobbs, 1998: Organization of precipitation along cold fronts. *Quart. J. Roy. Meteor. Soc.*, **124**, 649–652.
- Brown, S. A., J. D. Locatelli, M. T. Stoelinga, and P. V. Hobbs, 1999: Numerical modeling of precipitation cores on cold fronts. *J. Atmos. Sci.*, **56**, 1175–1196.
- Browning, K.A., 1990: Organization and internal structure of synoptic and mesoscale precipitation systems in midlatitudes. *Battan Memorial Volume*, Amer. Meteor. Soc., 433–460.
- Browning, K. A., and N. M. Roberts, 1996: Variation of frontal and precipitation structure along a cold front. *Quart. J. Roy. Meteor. Soc.*, **122**, 1845–1872.
- Browning, K. A., 2002: Mesoscale substructure of extratropical cyclones observed by radar. *Atlas Symposium*, Meteor. Monogr., Amer. Meteor. Soc., (in press).

- Carbone, R. E., 1982: Severe frontal rainband, Part I: Stormwide dynamic structure. *J. Atmos. Sci.*, **39**, 258-279.
- Charba, J., 1974: Application of gravity current model to analysis of squall-line gust front. *Mon. Wea. Rev.*, **102**, 140-156.
- Chen, C., C. H. Bishop, G. S. Lai, and W.-K. Tao, 1997: Numerical simulations of an observed narrow cold-frontal rainband. *Mon. Wea. Rev.*, **125**, 1027–1045.
- Dudhia, J., 1993: A nonhydrostatic version of the Penn State-NCAR mesoscale model: Validation tests and simulation of an Atlantic cyclone and cold front. *Mon. Wea. Rev.*, **121**, 1493-1513.
- Grell, G. A., 1993: Prognostic evaluation of assumptions used by cumulus parameterizations. *Mon. Wea. Rev.*, **121**, 764-787.
- Haurwitz, B., 1949: The instability of wind discontinuities and shear zones in planetary atmospheres. *J. Meteor.*, **6**, 200-206.
- Hobbs, P. V., 1978: Organization and structure of clouds and precipitation on the mesoscale and microscale in cyclonic storms. *Rev. Geophys. Space Phys.*, **16**, 741-755.
- Hobbs, P. V., and K. R. Biswas, 1979: The cellular structure of narrow cold-frontal rainbands. *Quart. J. Roy. Meteor. Soc.*, **105**, 723–727.
- Hobbs, P. V., and P. O. G. Persson, 1982: The mesoscale and microscale structure and organization of clouds and precipitation in mid-latitude cyclones. Part V: The substructure of narrow cold frontal rainbands. *J. Atmos. Sci.*, **39** 280-295.

- Houze, R. A., Jr., P. V. Hobbs, K. R. Biswas, and W. M. Davis, 1976: Mesoscale rainbands in extratropical cyclones. *Mon. Wea. Rev.*, **104**, 868-878.
- James, P. K., and K. A. Browning, 1979: Mesoscale structure of line convection at surface cold fronts. *Quart. J. Roy. Meteor. Soc.*, **105**, 371–382.
- Jorgensen, D. P., and B. F. Smull, 1993: Mesovortex circulations seen by airborne Doppler radar within a bow-echo mesoscale convective system. *Bull. Amer. Meteor. Soc.*, **74**, 2146-2157.
- Jorgensen, D. P., T. Matejka, and J. D. DuGranrut, 1996: Multi-beam techniques for deriving wind fields from airborne Doppler radars. *J. Meteor. Atmos. Phys.*, **59**, 83-104.
- Jorgensen, D. P., M. A. LeMone, and S. B. Trier, 1997: Structure and evolution of the 22 February 1993 TOGA COARE squall line: Aircraft observations of precipitation, circulation, and surface energy fluxes. *J. Atmos. Sci.*, **54**, 1961–1985.
- Jorgensen, D. P., and M. A. LeMone, 1989: Vertical velocity characteristics of oceanic convection. *J. Atmos. Sci.*, **46**, 621–644.
- Joss, J., and A. Waldvogel, 1970: Raindrop size distribution and Doppler velocities. *Preprints, 14th Conf. Radar Meteorology*, Amer. Meteor. Soc., Boston, MA, 153–156.
- Klemp, J. B., and R. B. Wilhelmson, 1978: The simulation of three dimensional convective storm dynamics. *J. Atmos. Sci.*, **35**, 1070-1096.
- Koch, S. E., 1984: The role of an apparent mesoscale frontogenetical circulation in squall line initiation. *Mon. Wea. Rev.*, **112**, 2090-2110.
- Koch, S. E., and P. J. Kocin, 1991: Frontal contraction processes leading to the formation of an intense narrow rainband. *Meteor. Atmos. Phys.*, **46**, 123-154.

- Koch, S. E., 1999: Comments on “Numerical simulations of an observed narrow cold frontal rainband”. *Mon. Wea. Rev.*, **127**, 252-257.
- Lafore, J.-P., and M. W. Moncrieff, 1989: A numerical investigation of the organization and interaction of the convective and stratiform regions of tropical squall lines. *J. Atmos. Sci.*, **46**, 521-544.
- LeMone, M. A., G. M. Barnes, E. J. Szoke, and E. J. Zipser, 1984: The tilt of the leading edge of mesoscale tropical convective lines. *Mon. Wea. Rev.* **112**, 510–519.
- LeMone, M. A., E. J. Zipser, and S. B. Trier, 1998: The role of environmental shear and thermodynamic conditions in determining the structure and evolution of mesoscale convective systems during TOGA COARE. *J. Atmos. Sci.*, **55**, 3493-3518.
- LeMone, M. A., and M. W. Moncrieff, 1994: Momentum and mass transport by convective bands: Comparisons of highly idealized dynamical models to observations. *J. Atmos. Sci.*, **51**, 281-305.
- Locatelli, J. D., J. E. Martin, and P. V. Hobbs, 1995: Development and propagation of precipitation cores on cold fronts. *Atmos. Res.*, **38**, 177-206.
- Parsons, D. B., C. G. Mohr, and T. Gal-Chen, 1987: A severe frontal rainband. Part III: Derived thermodynamic structure. *J. Atmos. Sci.*, **44**, 1615-1631.
- Parsons, D. B., 1992: An explanation of intense frontal updrafts and narrow cold-frontal rainbands. *J. Atmos. Sci.*, **49**, 1810-1825.
- Rotunno, R., J. B. Klemp, and M. L. Weisman, 1988: A theory for strong, long-lived squall lines. *J. Atmos. Sci.*, **45**, 463-485.

- Roux, F., V. Marícal, and D. Hauser, 1993: The 12/13 January 1988 narrow cold-frontal rainband observed during MFDP/FRONTS 87. Part I: Kinematics and thermodynamics. *J. Atmos. Sci.*, **50**, 951–974.
- Rutledge, S. A., and P. V. Hobbs, 1984: The Mesoscale and Microscale Structure and Organization of Clouds and Precipitation in Midlatitude Cyclones. Part XII: A Diagnostic Modeling Study of Precipitation Development in Narrow Cold-Frontal Rainbands. *J. Atmos. Sci.* **41**, 2949–2972.
- Simpson, J. E., and R. E. Britter, 1980: A laboratory model of an atmospheric mesofront. *Quart. J. Roy. Meteor. Soc.*, **106**, 485-500.
- Thorpe, A. J., M. J. Miller, and M. W. Moncrieff, 1982: Two-dimensional convection in non-constant shear: A model of midlatitude squall lines. *Quart. J. Meteor. Soc.*, **108**, 739-762.
- Wakimoto, R. M., B. L. Bosart, 2000: Airborne radar observations of a cold front during FASTEX. *Mon. Wea. Rev.* **128**, 2447–2470.
- Weisman, M. L., J. B. Klemp, and R. Rotunno, 1988: Structure and evolution of numerically simulated squall lines. *J. Atmos. Sci.* **45**, 1990-2013.
- Weisman, M. L., and J. B. Klemp, 1982: The dependence of numerically simulated convective storms on vertical wind shear and buoyancy. *Mon. Wea. Rev.*, **110**, 504–520.
- Weisman, M. L., 1993: The genesis of severe, long-lived bow-echoes. *J. Atmos. Sci.*, **50**, 645-670.

Zhang, D.-L., and R. A. Anthes, 1982: A high-resolution model of the planetary boundary layer—Sensitivity tests and comparisons with SESAME-79 data. *J. Appl. Meteor.*, **21**, 1594-1609.

Table 1. Characteristics of the NOAA P-3s weather radars.

Parameter	Doppler Tail Radar	Lower Fuselage Radar
Antenna Rotation Radar ($^{\circ}\text{s}^{-1}$)	60	12
Transmitter wavelength (cm)	3.22	5.59
Transmitter pulse length (μsec)	0.5, 0.375, or 0.25	6
Receiver minimum detectable signal (dBm)	-111	-109
Pulse Repetition Frequency (Hz)	3200/2133	200
Sweep angle resolution ($^{\circ}$)	0.6	1.92
Peak transmitted power (kW)	60	70
Horizontal beam width ($^{\circ}$)	2.02	1.35
Vertical beam width ($^{\circ}$)	2.04	4.1
Gain, main beam (dB)	40	37.5
Gain, sidelobes (dB)	Hor: -56.6; Ver: -41.6	-23.0
Pulses averaged per radial	32	32
Nyquist (unambiguous) velocity (m s^{-1})	51.6	
Nyquist (unambiguous) range (km)	46.8	749.5
Gate spacing (m)	150	750

Figure Captions

- Fig. 1 Scanning geometry of the NOAA P-3 tail-mounted X-band Doppler radar. The antenna scans alternatively looking forward and then aft 20° from a plane perpendicular to the aircraft's longitudinal axis (top figure). The bottom plot shows the projection of the fore and aft scans on a horizontal plane. Where the beams intercept, a horizontal wind estimate can be made. The horizontal data spacing of intersecting beams is proportional to the product of the aircraft's ground speed and antenna rotation rate. For the P-3, with a 10 RPM rotation rate and ~ 120 m/s ground speed, the spacing is nominally ~ 1.4 km. If the antenna is scanned toward only one side of the aircraft (sector scanning) the spacing can be reduced to ~ 700 m.
- Fig. 2 Geopotential height (10s of meters, solid line) and temperature (K, dashed line) analyses at 500 kPa for 19 February 2001.
- Fig. 3 Surface analyses for 0600 UTC 19 February 2001.
- Fig. 4 Infrared satellite images from the GOES-10 satellite at 0400 UTC 19 February 2001. The color scale for cloud top temperature ($^\circ\text{C}$) is shown at the bottom of the plot. The black line indicates the approximate location of the NCFR from the P-3s lower fuselage radar.
- Fig. 5 SkewT-Log P plot of a composite sounding made up of a P-3 dropsonde from 500 hPa at 0234 UTC with the 0000 UTC radiosonde launched at Oakland, California. Dropsonde was located near 34.0°N , 124.8°W , about ~ 150 km ahead of the NCFR.

Fig. 6 Radar reflectivity composite of 68 scans from the P-3's lower fuselage radar from 0520-0554 UTC 19 February 2001. The P-3 track is indicated by the white line, the two psuedo-dual-Doppler analysis domains by the two black boxes with tic marks labeled "A" and "B", and the reflectivity color scale (dBZ) is indicated by the scale on the right side of the panel. The locations of aircraft spiral ascents/descents are indicated by the spiral flight tracks. The locations of three possible NCFR "breaks" are also indicated.

Fig. 7 Wind components (top figure m s^{-1}) from the three P-3 ascent/descent soundings the locations of which are shown in Fig. 6. The u (east-west) component is shown for the post-frontal sounding; the v (north-south) component is shown for the pre-frontal soundings. Bottom figure is the equivalent potential temperature (K).

Fig. 8 Horizontal storm-relative winds and reflectivity field at 1.0 km MSL from the airborne pseudo-dual-Doppler analysis for the region labeled "A" in Fig. 6. P-3 flight track is shown as the thin red line running approximately south to north near the right hand side of the plot. The shaded lines running approximately East-West and labeled A-A' and B-B' indicates the locations of vertical cross sections. The radar reflectivity color scale is shown to the right. The grid was moved with the mean line motion, toward 53° at 18 m s^{-1} .

Fig. 9 As in Fig. 8, except for 1.75 km MSL.

Fig. 10 As in Fig. 8, except for the pseudo-dual-Doppler analysis for the region labeled "B" in Fig. 6

- Fig. 11 As in Fig. 10, except for the 1.75 km MSL.
- Fig. 12 Vertical cross section of radar reflectivity and system relative winds in the plane of the cross section for the sections labeled A-A' (top panel) and B-B' (bottom panel) in Fig. 8. The vertical wind scale has been stretched to match the plot aspect ratio. Reflectivity color scale and wind scale are at the top of each figure.
- Fig. 13 Schematic diagram showing the various responses of a convective updraft to various strengths of the environmental low-level wind shear and cold pool. The sense of the circulations (i.e., horizontal vorticity) associated with the wind shear and cold pool are depicted by circular arrows. The thick, double-lined red arrow denotes the updraft current. Blue shading denotes the cold pool. Rainfall regions are indicated by light vertical lines with the outline of the cloud indicated by the shaded, scalloped lines. [From Weisman (1993).]
- Fig. 14 Vertical profiles of mean cross section cross-frontal wind velocity within the prefrontal regions ahead of the surface frontal position derived from pseudo-dual-Doppler observations. The blue line labeled A-A' represents conditions near the part of the NCFR just north of the break shown in Fig. 7, while the red line labeled B-B' represents conditions to the south of the NCFR. The averaging domains are 5 km by 10 km boxes ahead of the NCFR centered on the western end point of the two cross sections A-A' and B-B'.
- Fig. 15 Horizontal storm-relative winds and reflectivity field at 0.5 km MSL from the airborne pseudo-dual-Doppler analysis for both regions labeled "A" and "B" in Fig. 6. The P-3 flight track is shown as the thin red line running approximately south to north near the

right hand side of the plot. . The heavy black line connects the ribbon of maximum vertical velocity. Regions where the updraft is to the west of the rainfall maxima are designated “downshear” zones, regions where updraft and reflectivity cores are coincident are labeled “erect”, and regions where updrafts are to the east of reflectivity cores are labeled “upshear”.

Fig. 16 Horizontal view of 4 km grid mesh system relative flow and precipitation (mm h^{-1}) at 850 hPa valid at 0500 UTC 19 February 2001 after 17 hours of integration.

Precipitation is from the previous hours accumulation with the color scale to the right of the plot.

Fig. 17 Surface model precipitation (mm h^{-1}) for the 5 hour period from 13 to 18 hours after initialization (0100 UTC to 0600 UTC 19 February 2001) from the 4 km grid.

Fig. 18 Horizontal plot of model surface equivalent potential temperature (solid contours every 2 K) and system relative wind at 1 km MSL (system motion $u=12.8 \text{ m s}^{-1}$, $v=15.4 \text{ m s}^{-1}$) and surface precipitation (shaded contours mm h^{-1}) on the 1.3 km grid at 0600 UTC 19 February 2001. The color scale for the precipitation shading is shown to the right of the plot. The scaling vector for a 20 m s^{-1} vector is shown above the precipitation color scale. The boxes labeled B1 through B8 are averaging regions for vertical profiles shown in Fig. 19.

Fig. 19 Vertical profiles of (a) mean u (cross frontal) wind component (m s^{-1}), (b) mean v (along frontal) wind component (m s^{-1}), (c) mean vertical motion (m s^{-1}), and (d) equivalent potential temperature (K) for the regions shown in Fig. 15. Solid contours

are for regions (B1 – B4) behind the NCFR while dashed contours are for regions (B5 – B8) ahead of the front.

Fig. 20 Cross-frontal wind component (m s^{-1}) from the two P-3 ascent/descent soundings ahead of the NCFR shown in Fig. 6. The blue line is the northern most sounding, the red line the southernmost sounding.

Fig. 21 Vertical cross section of model reflectivity (dBZ) and vertical velocity (cm s^{-1}) along an east-west line through the NCFR leading edge.

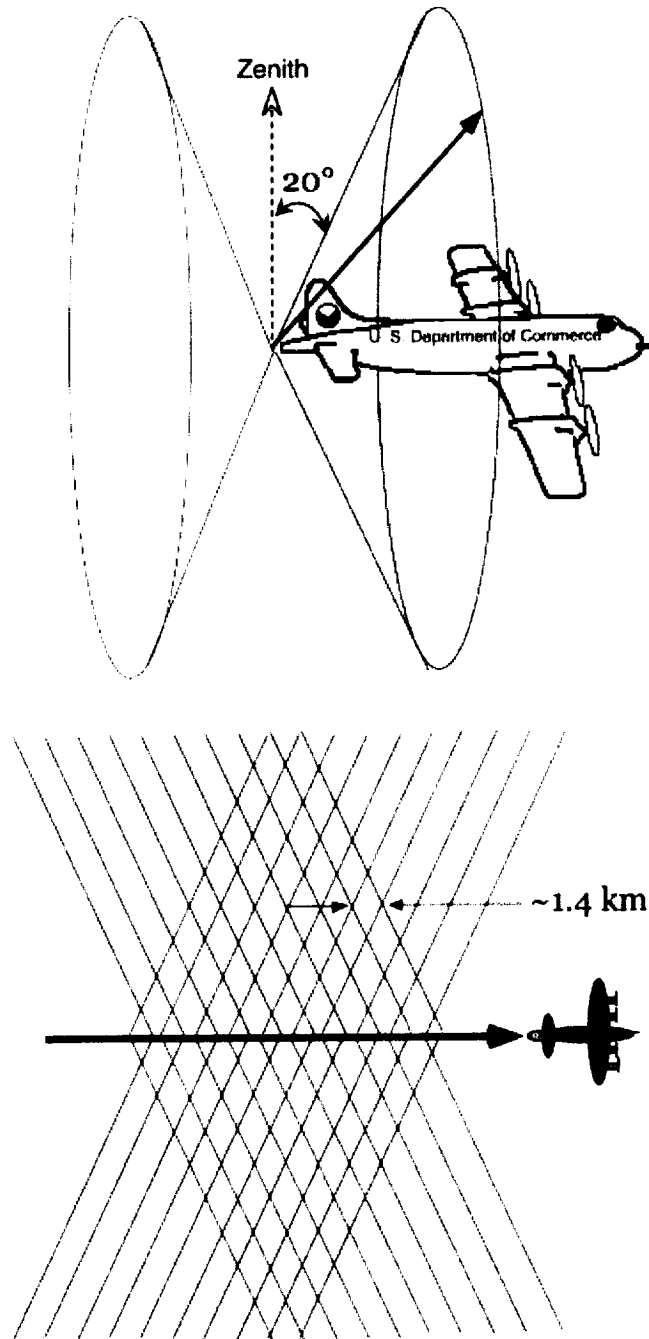


Fig. 1 Scanning geometry of the NOAA P-3 tail-mounted X-band Doppler radar. The antenna scans alternatively looking forward and then aft 20° from a plane perpendicular to the aircraft's longitudinal axis (top Fig.). The bottom plot shows the projection of the fore and aft scans on a horizontal plane. Where the beams intercept, a horizontal wind estimate can be made. The horizontal data spacing of intersecting beams is proportional to the product of the aircraft's ground speed and antenna rotation rate. For the P-3, with a 10 RPM rotation rate and ~ 120 m/s ground speed, the spacing is nominally ~ 1.4 km. If the antenna is scanned toward only one side of the aircraft (sector scanning) the spacing can be reduced to ~ 700 m.

02/19/2001 00 UTC 500 kPa Analysis Heights/Temperature

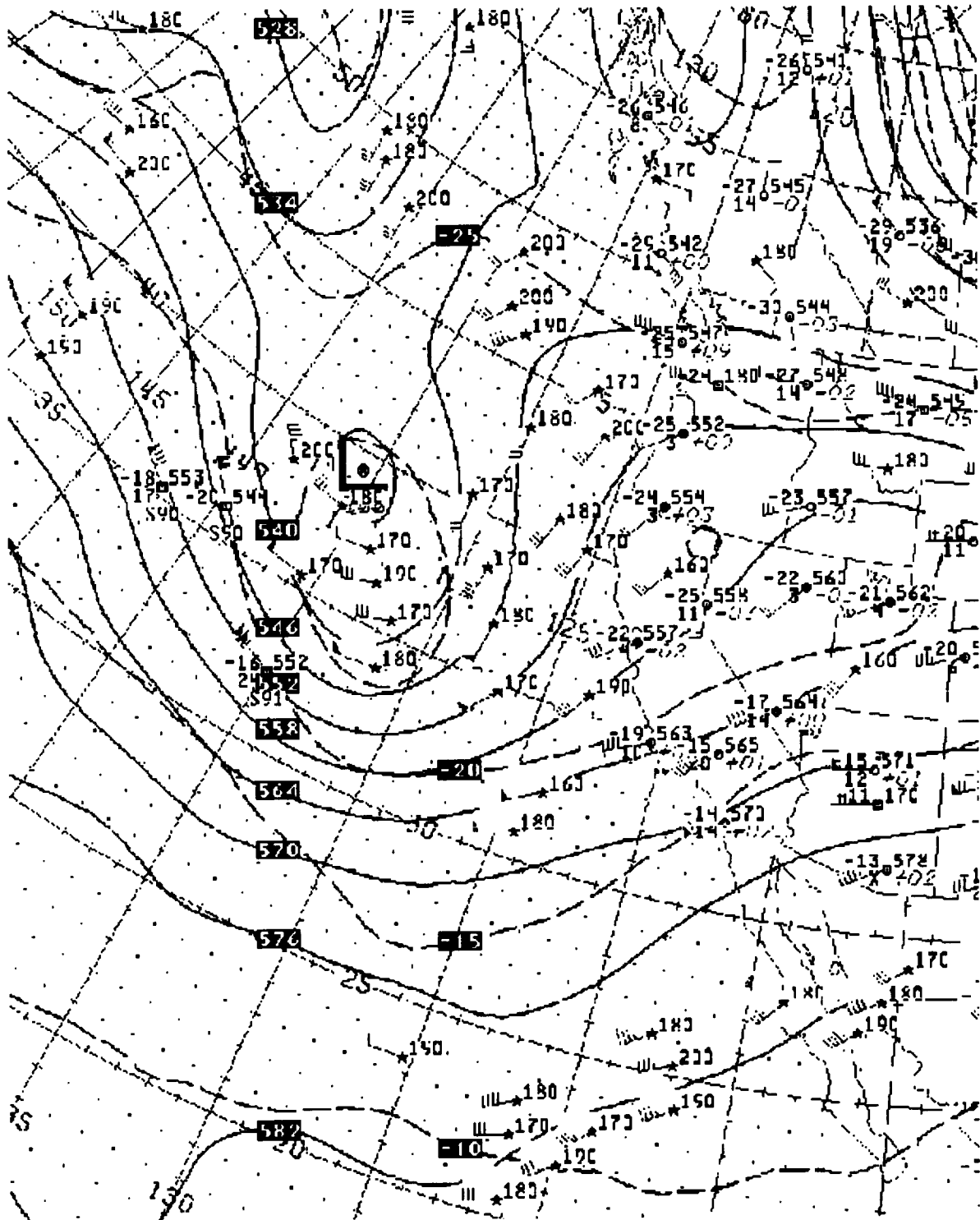
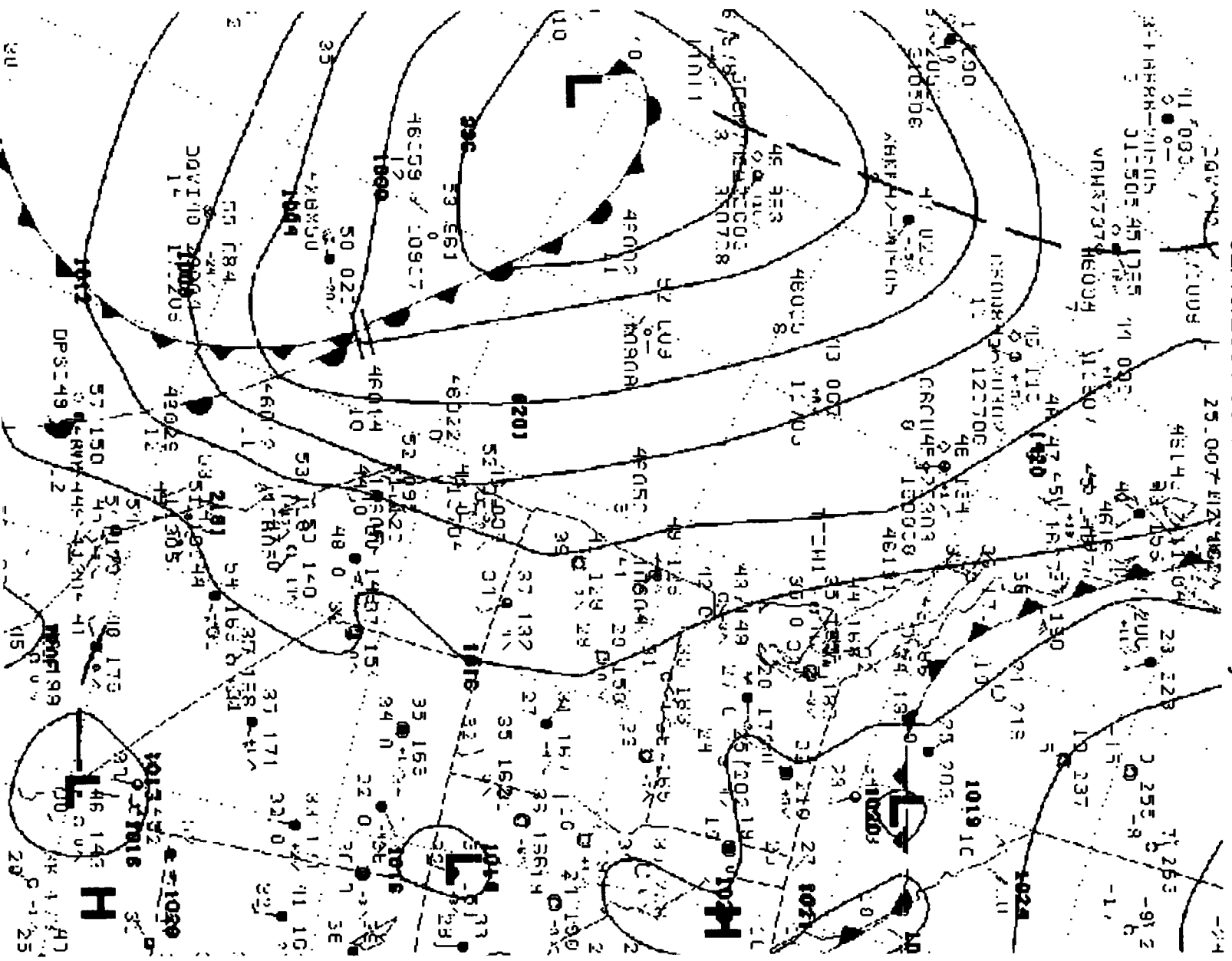


Fig. 2 Geopotential height (10s of meters, solid line) and temperature (K, dashed line) analyses at 500 kPa for 19 February 2001.

02/19/2001 06 UTC Surface Analysis



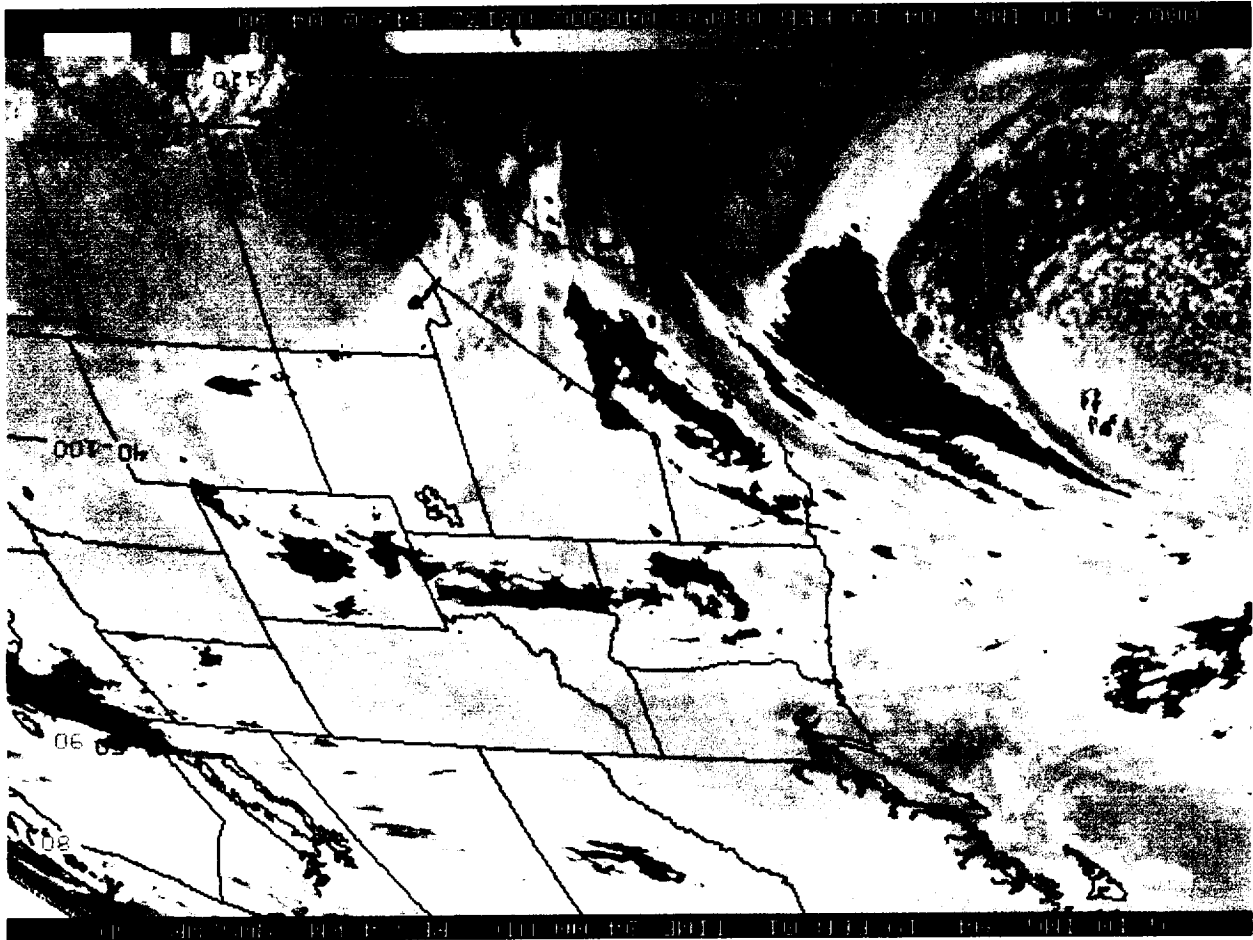


Fig. 4 Infrared satellite images from the GOES-10 satellite at 0400 UTC 19 February 2001. The color scale for cloud top temperature ($^{\circ}\text{C}$) is shown at the bottom of the plot. The black line indicates the approximate location of the NCFR from the P-3s lower fuselage radar.

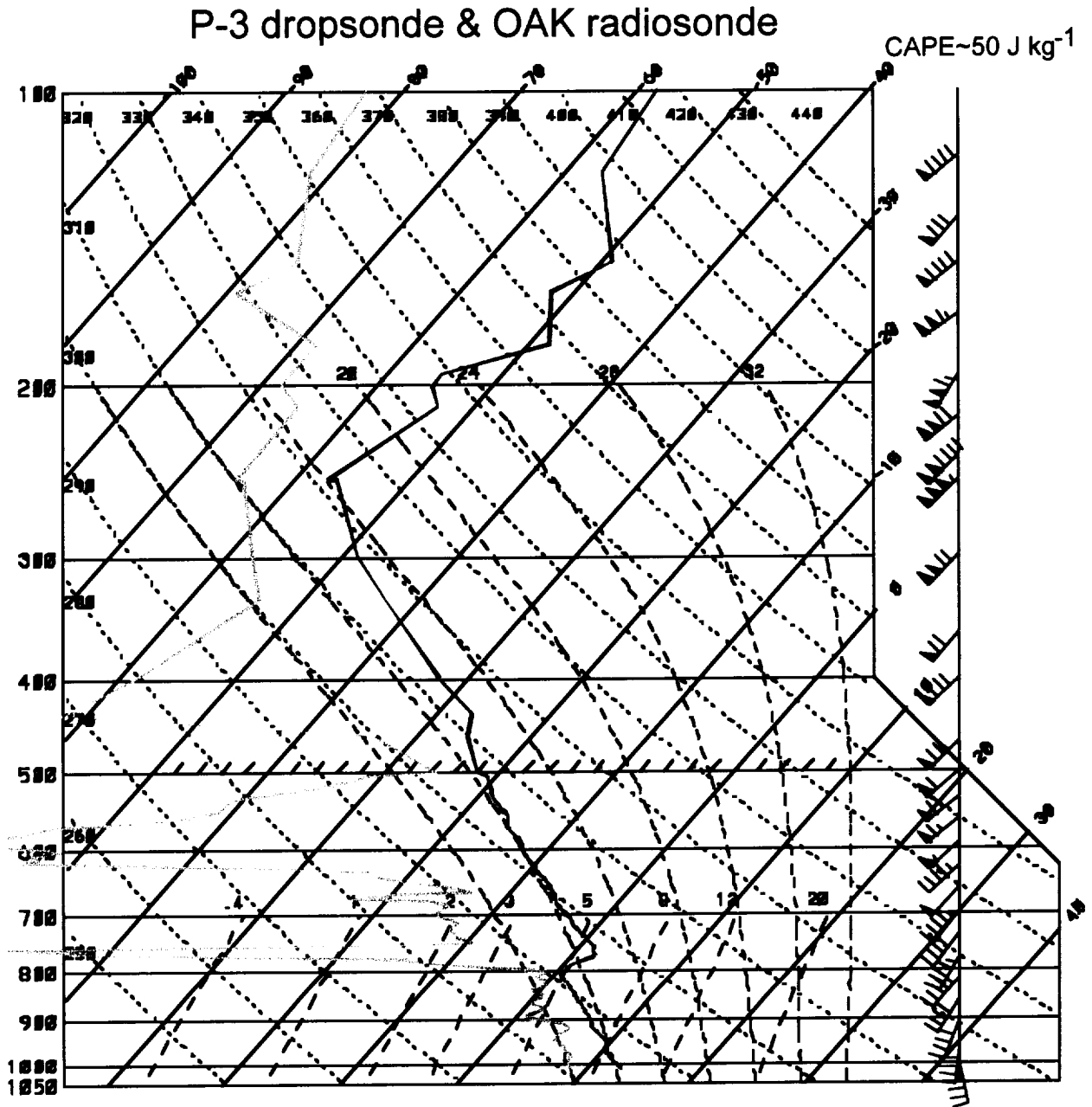


Fig. 5 SkewT-Log P plot of a composite sounding made up of a P-3 dropsonde from 500 hPa at 0234 UTC with the 0000 UTC radiosonde launched at Oakland, California. Dropsonde was located near 34.0 N, 124.8 W, about ~150 km ahead of the NCFR.

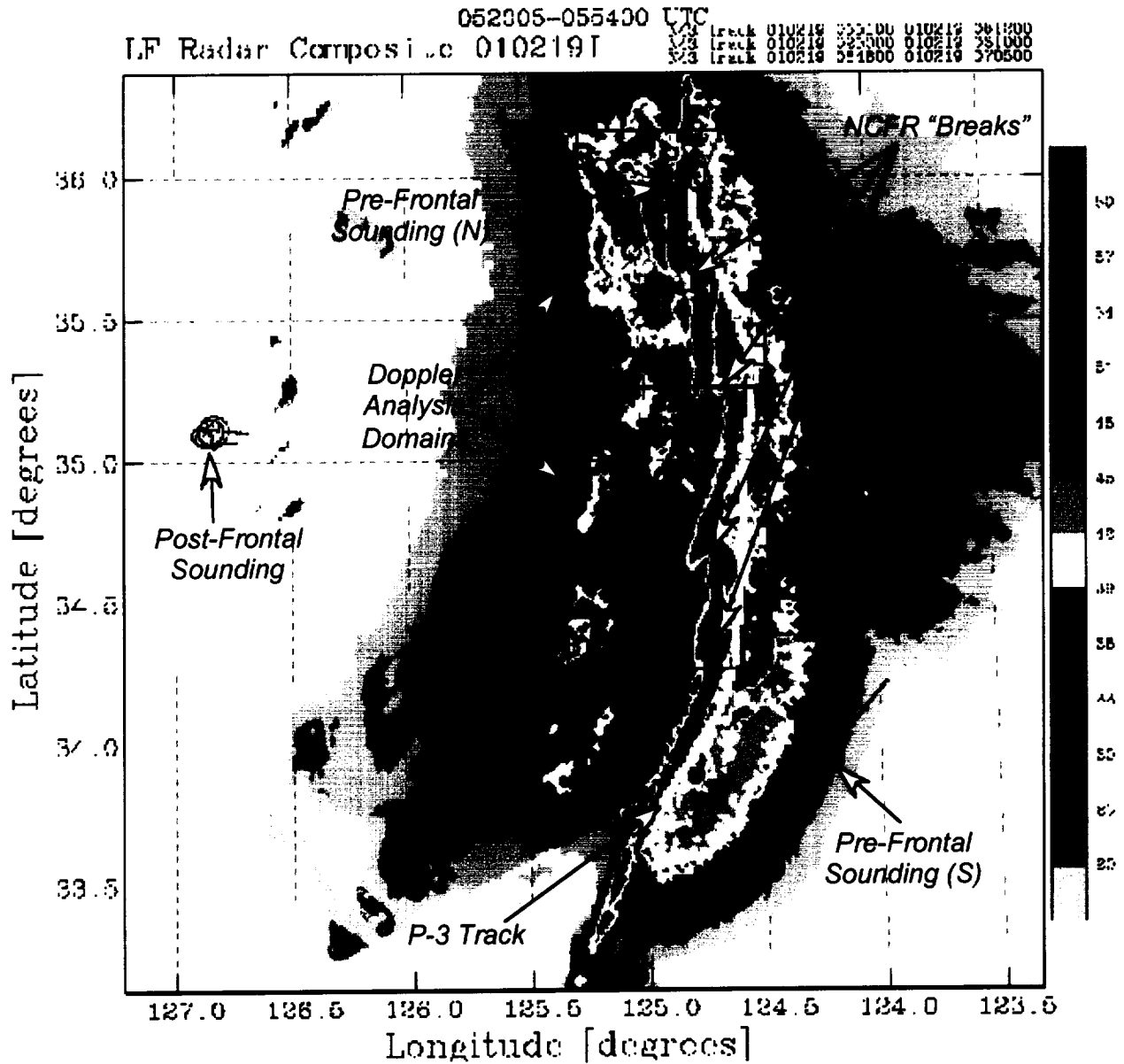


Fig. 6 Radar reflectivity composite from the P-3's lower fuselage radar from 0520-0554 UTC 19 February 2001. The P-3 track is indicated by the white line, the pseudo-dual-Doppler analysis domains by the two black boxes with tic marks labeled "A" and "B", and the reflectivity color scale (dBZ) is indicated by the scale on the right side of the panel. The locations of aircraft spiral ascents/descents are indicated by the spiral flight tracks. The locations of three possible NCFR "breaks" are also indicated.

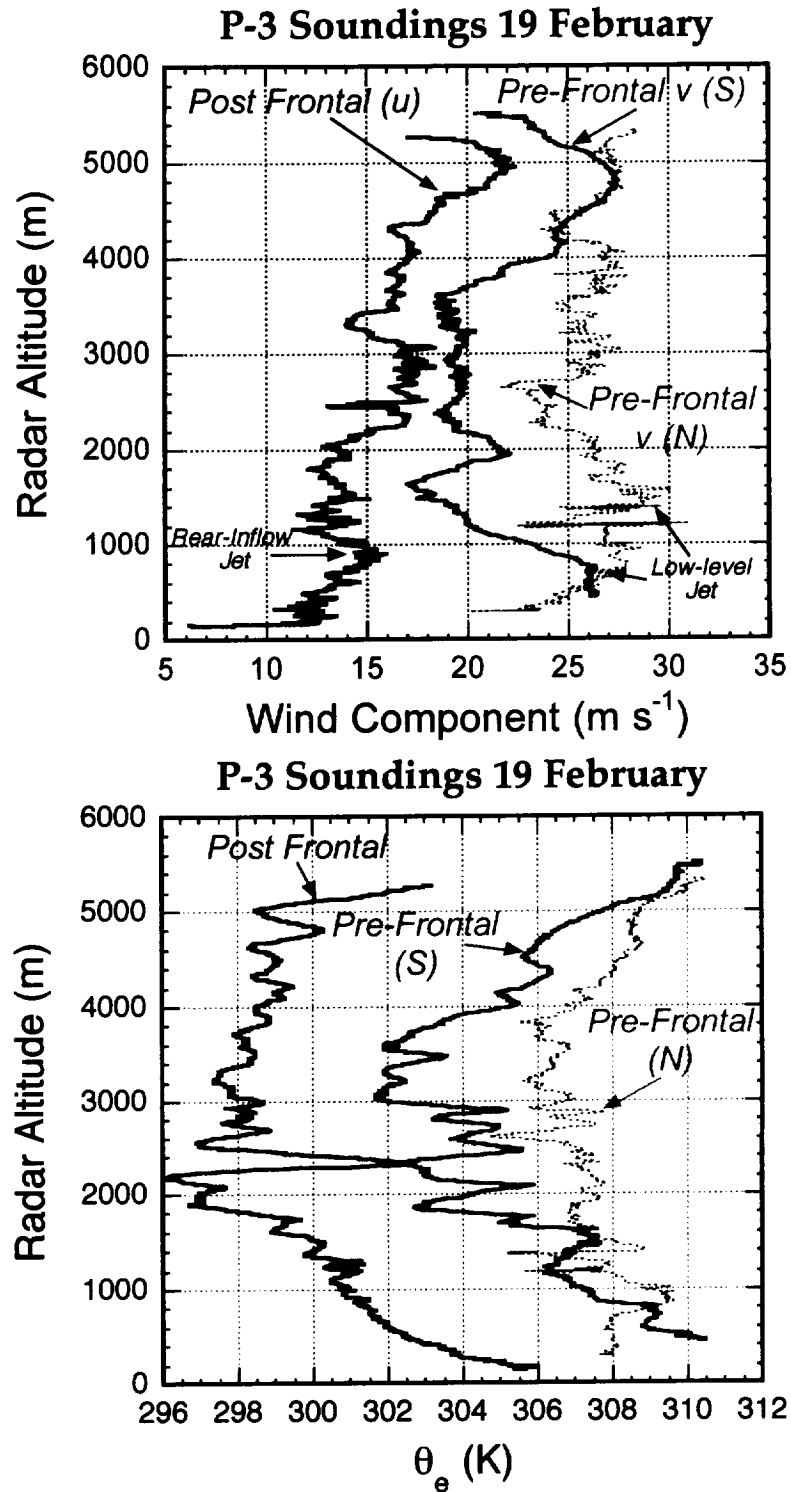


Fig. 7 Wind components (top plot m s^{-1}) from the three P-3 ascent/descent soundings the locations of which are shown in Fig. 6. The u (east-west) component is shown for the post-frontal sounding; the v (north-south) component is shown for the pre-frontal soundings. Bottom plot is the equivalent potential temperature (K).

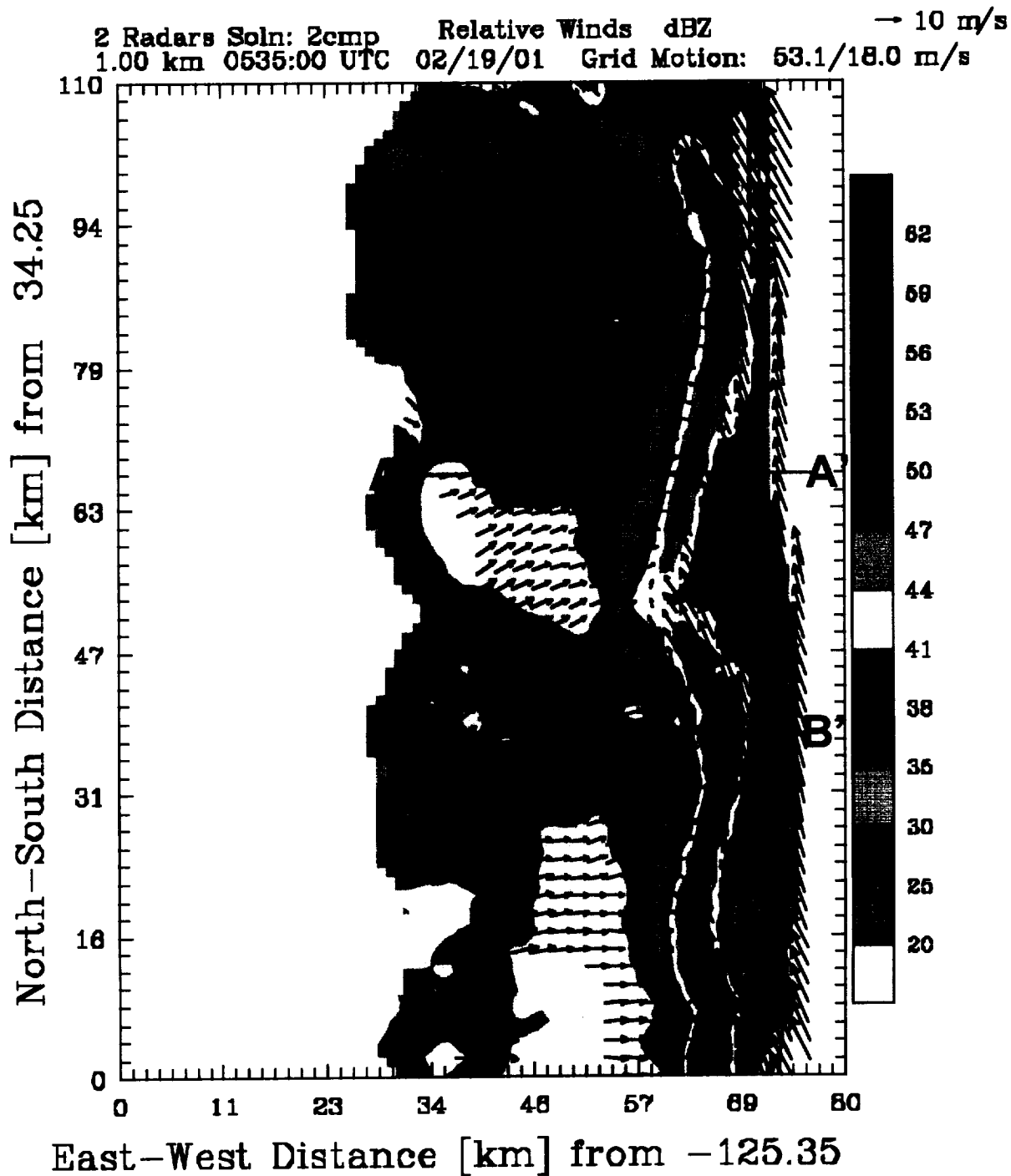


Fig. 8 Horizontal storm-relative winds and reflectivity field at 1.0 km MSL from the airborne pseudo-dual-Doppler analysis for the region labeled "A" in Fig. 6. P-3 flight track is shown as the thin red line running approximately south to north near the right hand side of the plot. The shaded lines running approximately East-West and labeled A-A' and B-B' indicate the locations of vertical cross sections. The radar reflectivity color scale is shown to the right and the wind scale at the top. The grid was moved with the mean line motion, toward 53° at 18 m s^{-1} .

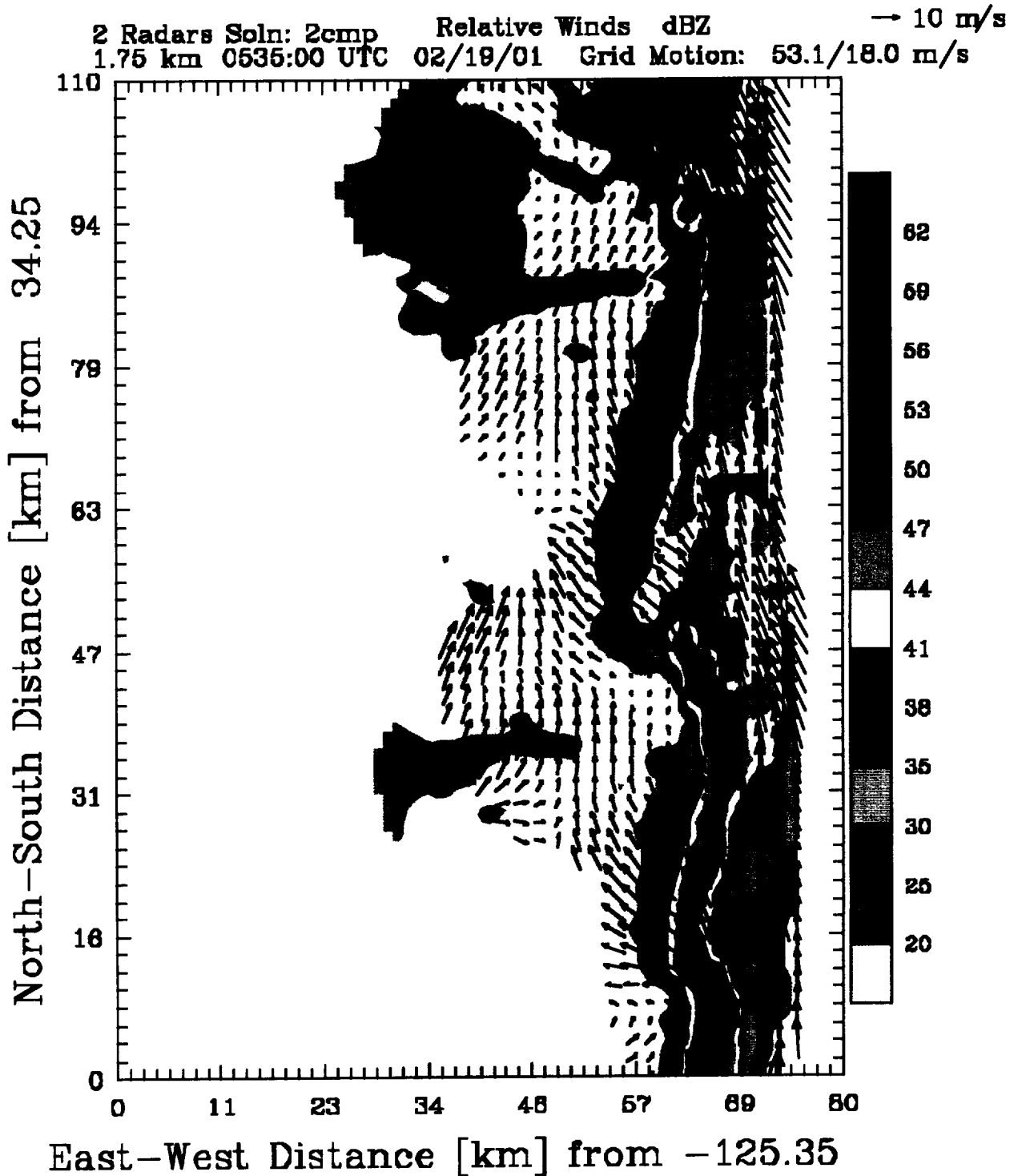


Fig. 9 As in Fig. 8, except for 1.75 km MSL.

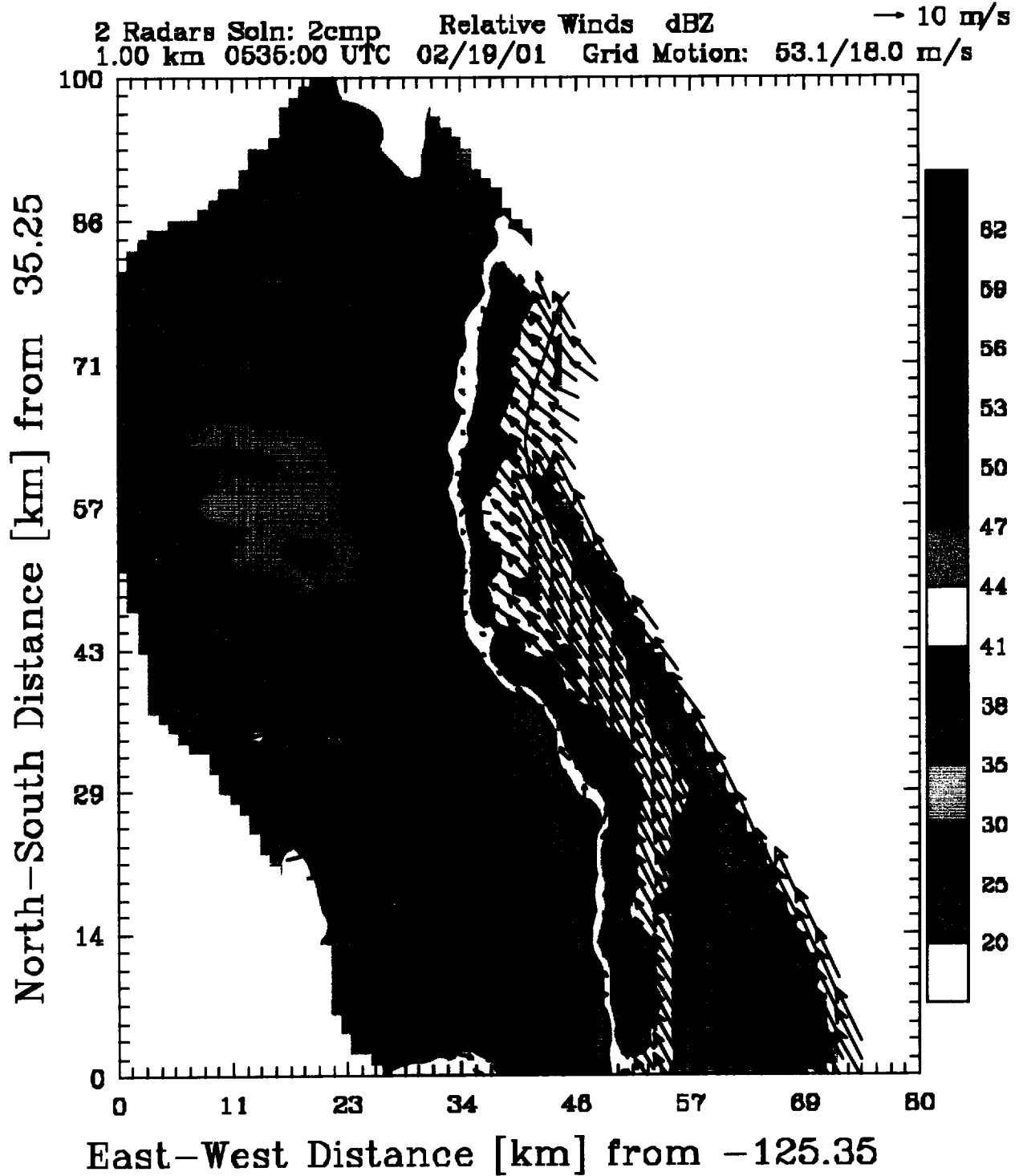


Fig. 10 As in Fig. 7, except for the pseudo-dual-Doppler analysis for the region labeled "B" in Fig. 6.

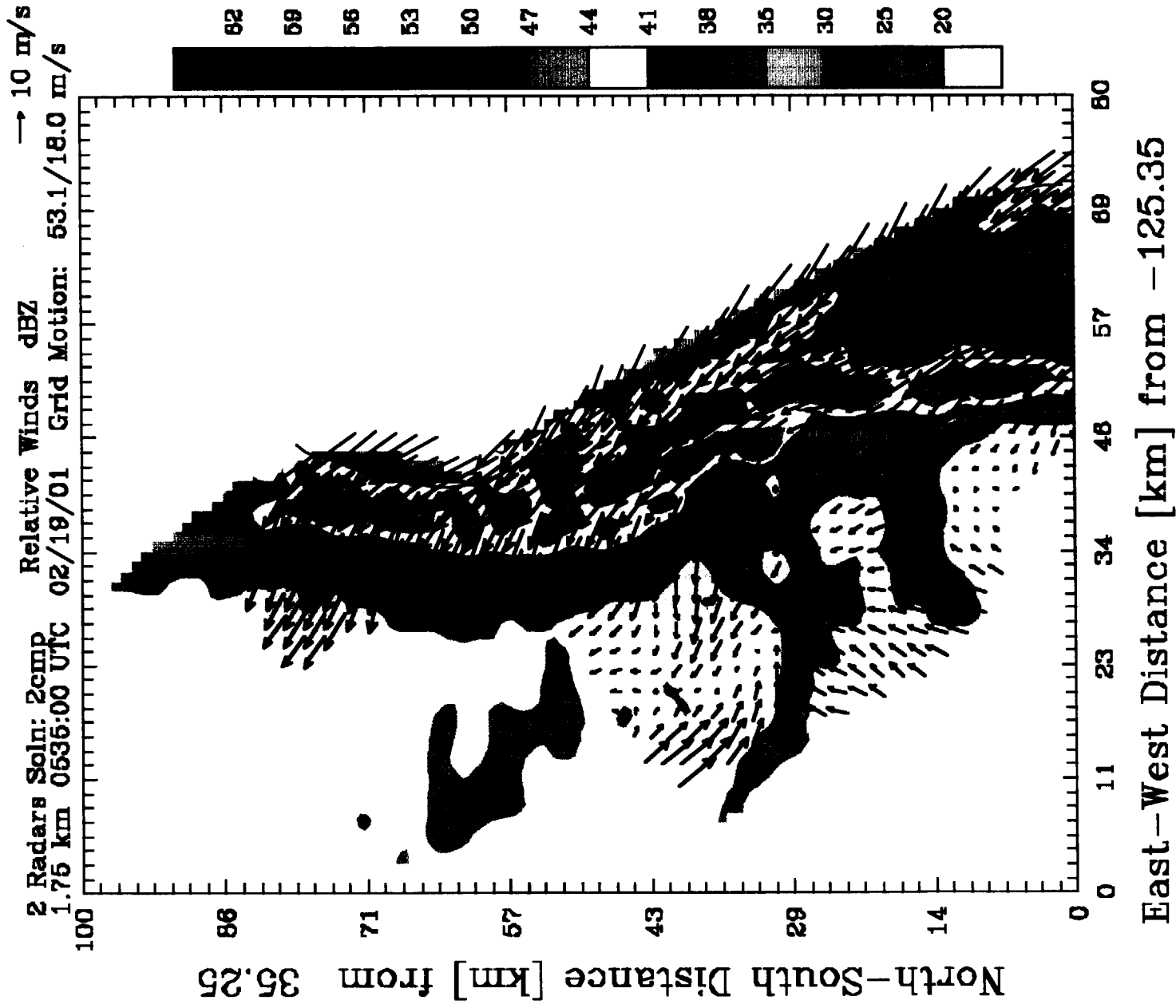


Fig. 11 As in Fig. 10, except for the 1.75 km MSL.

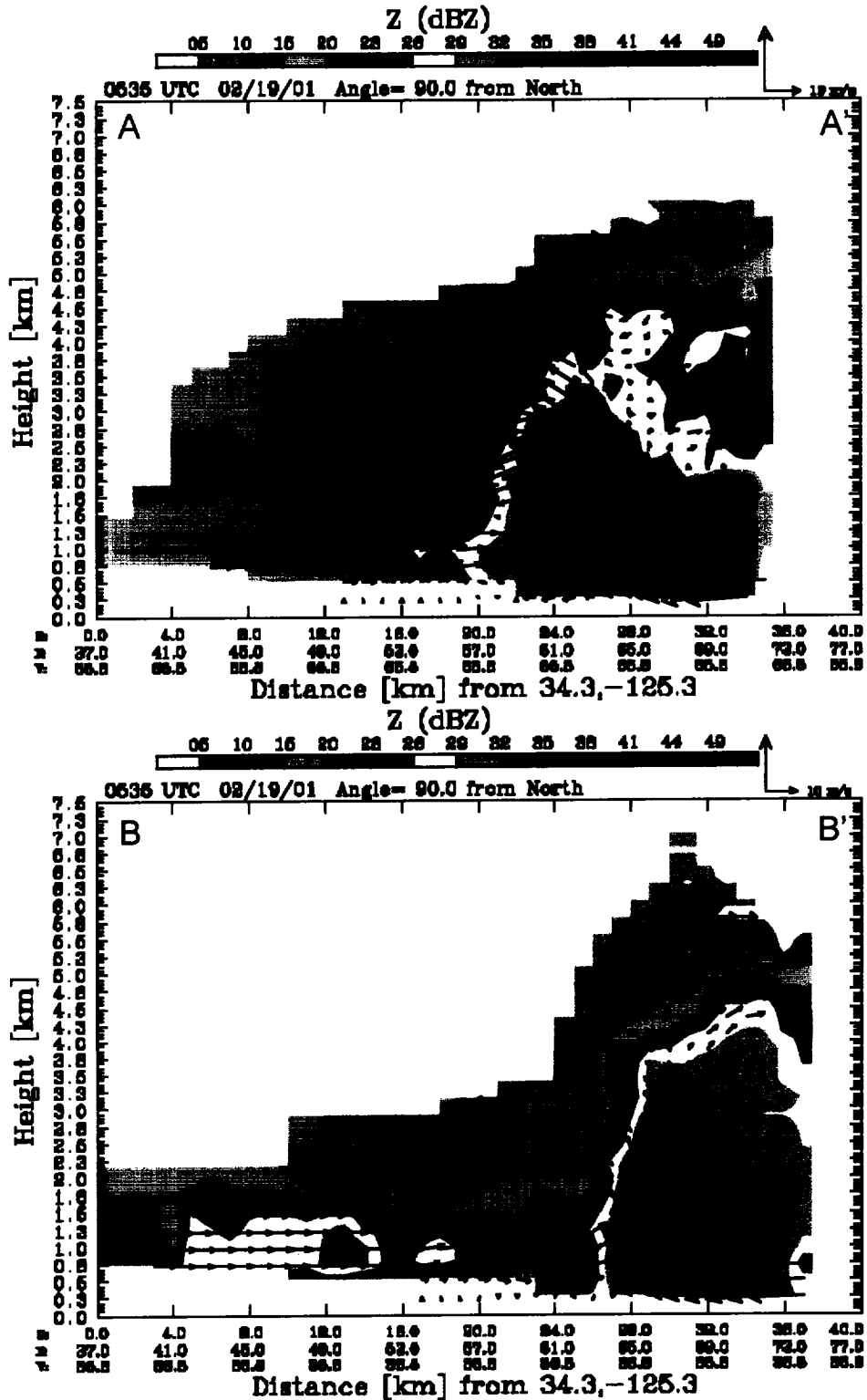


Fig. 12 Vertical cross section of radar reflectivity and system relative winds in the plane of the cross section for the sections labeled A-A' (top panel) and B-B' (bottom panel) in Fig. 8. The vertical wind scale has been stretched to match the plot aspect ratio. Reflectivity color scale and wind scale are at the top of each Fig..

EVOLUTIONARY STAGES

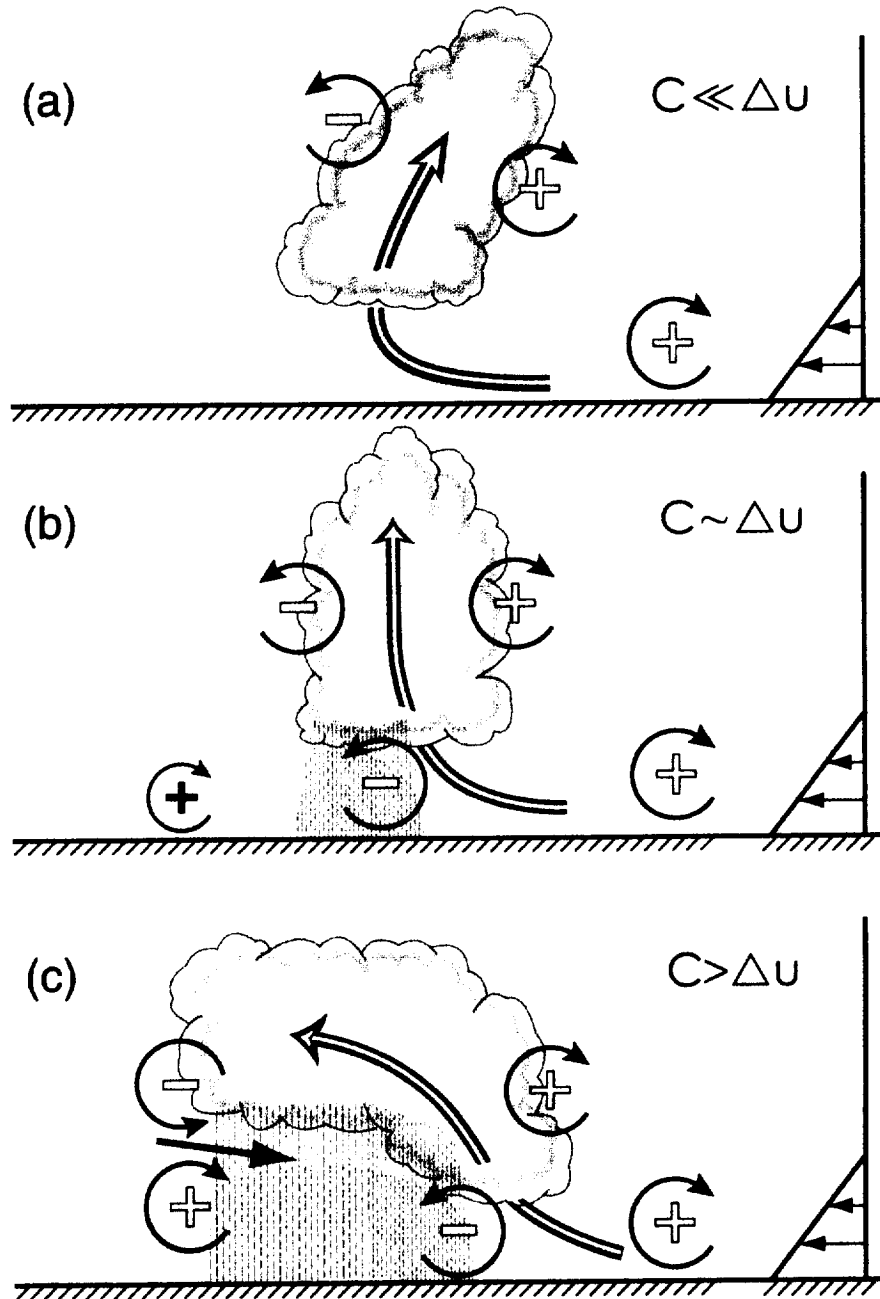


Fig. 13 Schematic diagram showing the various responses of a convective updraft to various strengths of the environmental low-level wind shear and cold pool. The sense of the circulations (i.e., horizontal vorticity) associated with the wind shear and cold pool is depicted by circular arrows. The thick, double-lined red arrow denotes the updraft current. Blue shading denotes the cold pool. Rainfall regions are indicated by light vertical lines with the outline of the cloud indicated by the shaded, scalloped lines. [From Weisman (1993).]

Prefrontal Shear

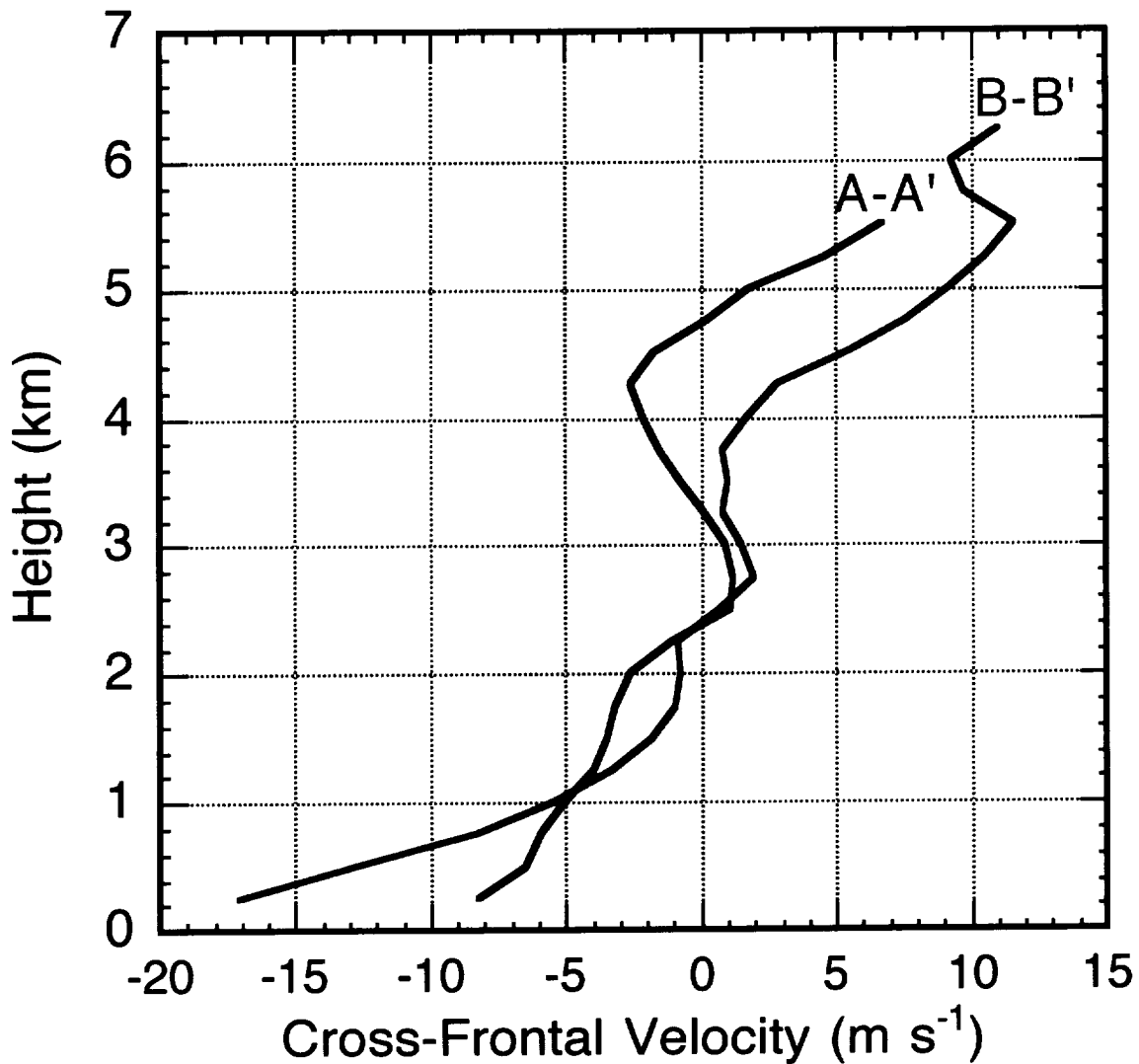


Fig. 14 Vertical profiles of mean cross section cross-frontal wind velocity within the prefrontal regions ahead of the surface frontal position derived from pseudo-dual-Doppler observations. The blue line labeled A-A' represents conditions near the part of the NCFR just north of the break shown in Fig. 8, while the red line labeled B-B' represents conditions to the south of the NCFR. The averaging domains are 5 km by 10 km boxes ahead of the NCFR centered on the western end point of the two cross sections A-A' and B-B'.

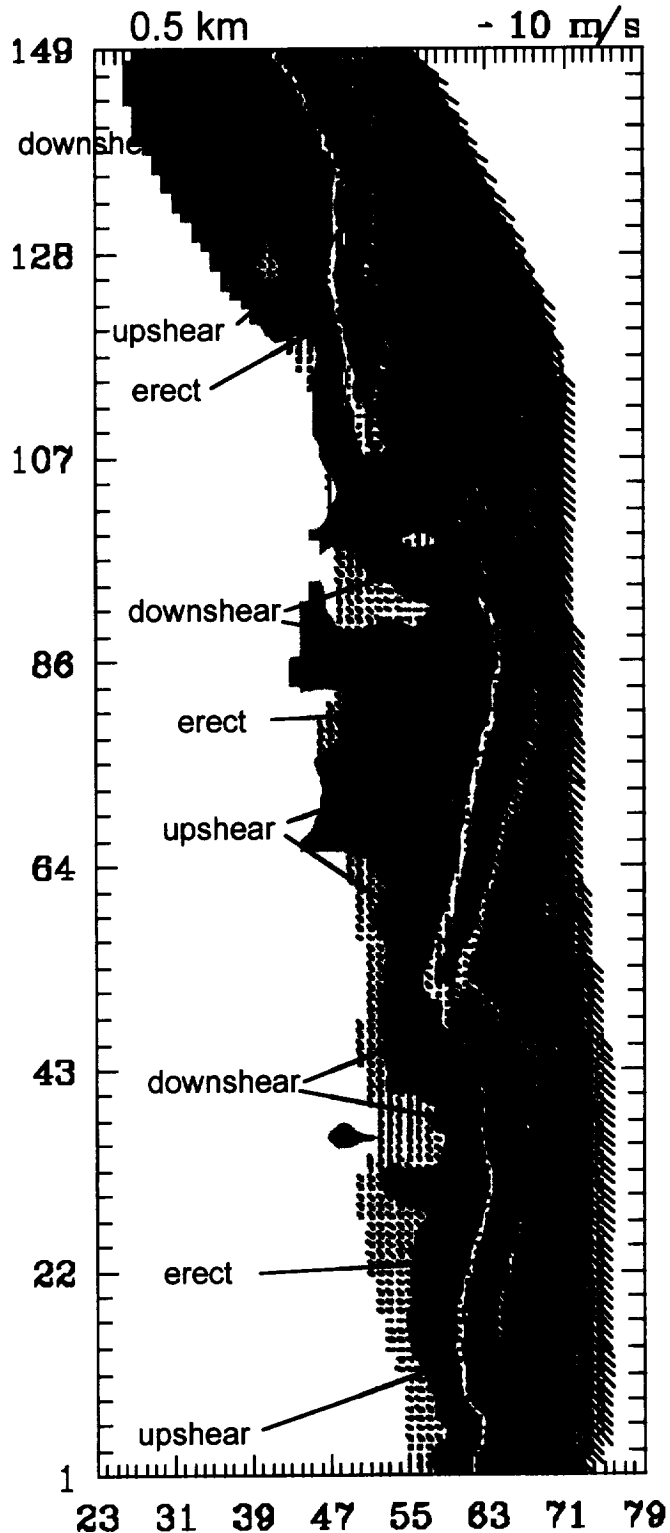


Fig. 15 Horizontal storm-relative winds and reflectivity field at 0.5 km MSL from the airborne pseudo-dual-Doppler analysis for both regions labeled "A" and "B" in Fig. 6. The P-3 flight track is shown as the thin red line running approximately south to north near the right hand side of the plot. The heavy black line connects the ribbon of maximum

vertical velocity. Regions where the updraft is to the west of the rainfall maxima are designated “downshear” zones, regions where updraft and reflectivity cores are coincident are labeled “erect”, and regions where updrafts are to the east of reflectivity cores are labeled “upshear”.

MM5 4 km grid

Precipitation (mm h^{-1}) - System Relative Winds at 850 mb

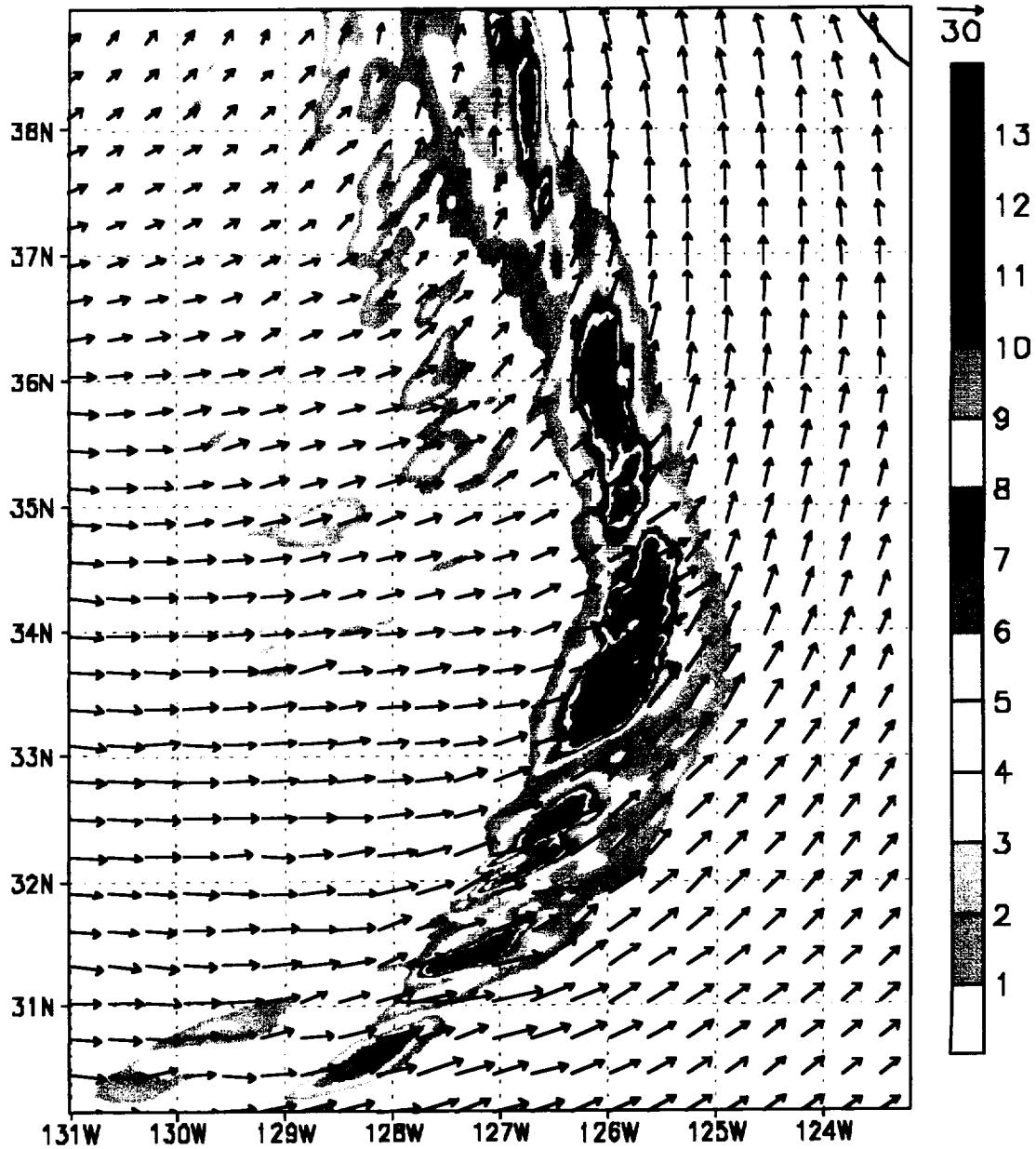


Fig. 16 Horizontal view of 4 km grid mesh system relative flow and precipitation (mm h^{-1}) at 850 hPa valid at 0500 UTC 19 February 2001 after 17 hours of integration. Precipitation is from the previous hours accumulation with the color scale to the right of the plot.

precip 13~18 h (4km grids)

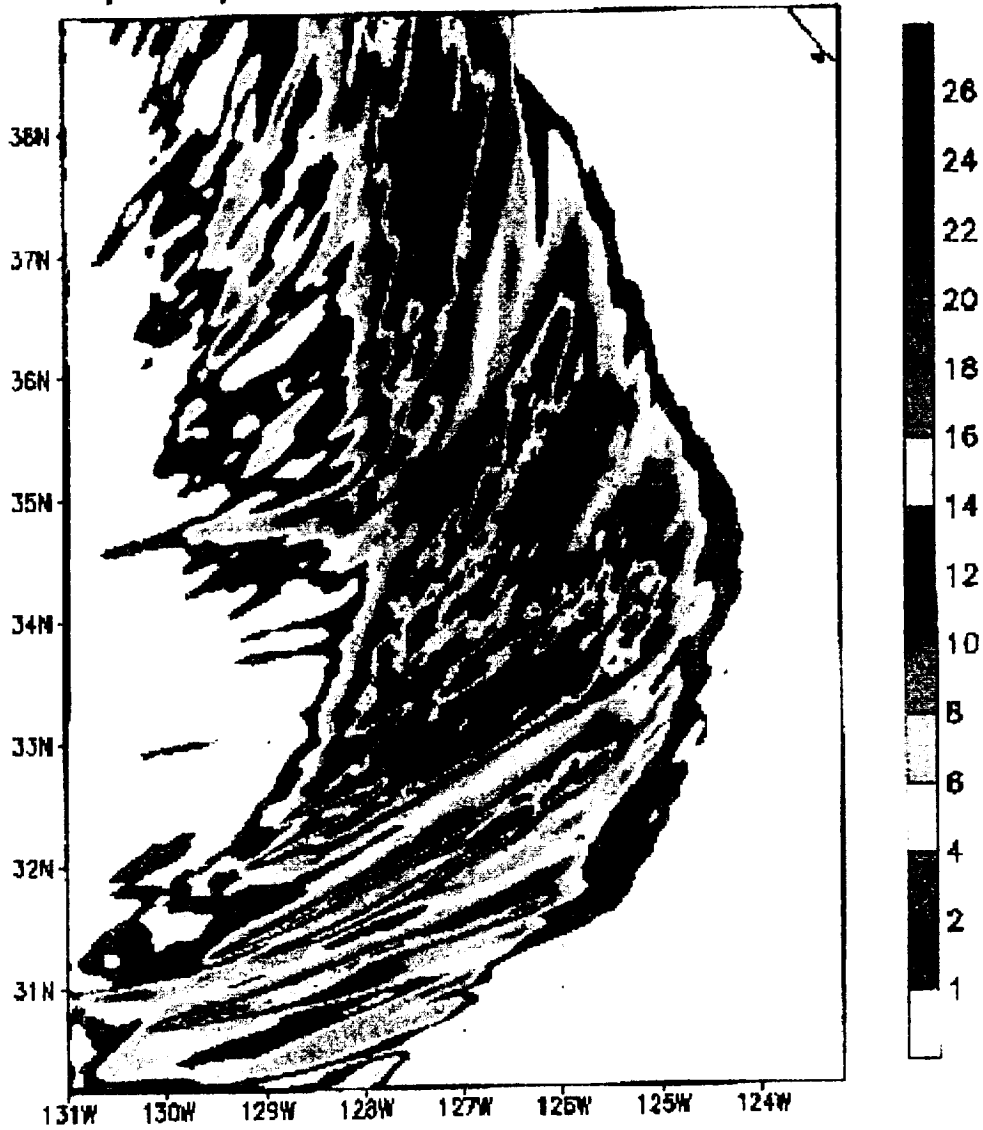


Fig. 17 Surface model precipitation (mm h^{-1}) for the 5 hour period from 13 to 18 hours after initialization (0100 UTC to 0600 UTC 19 February 2001) from the 4 km grid.

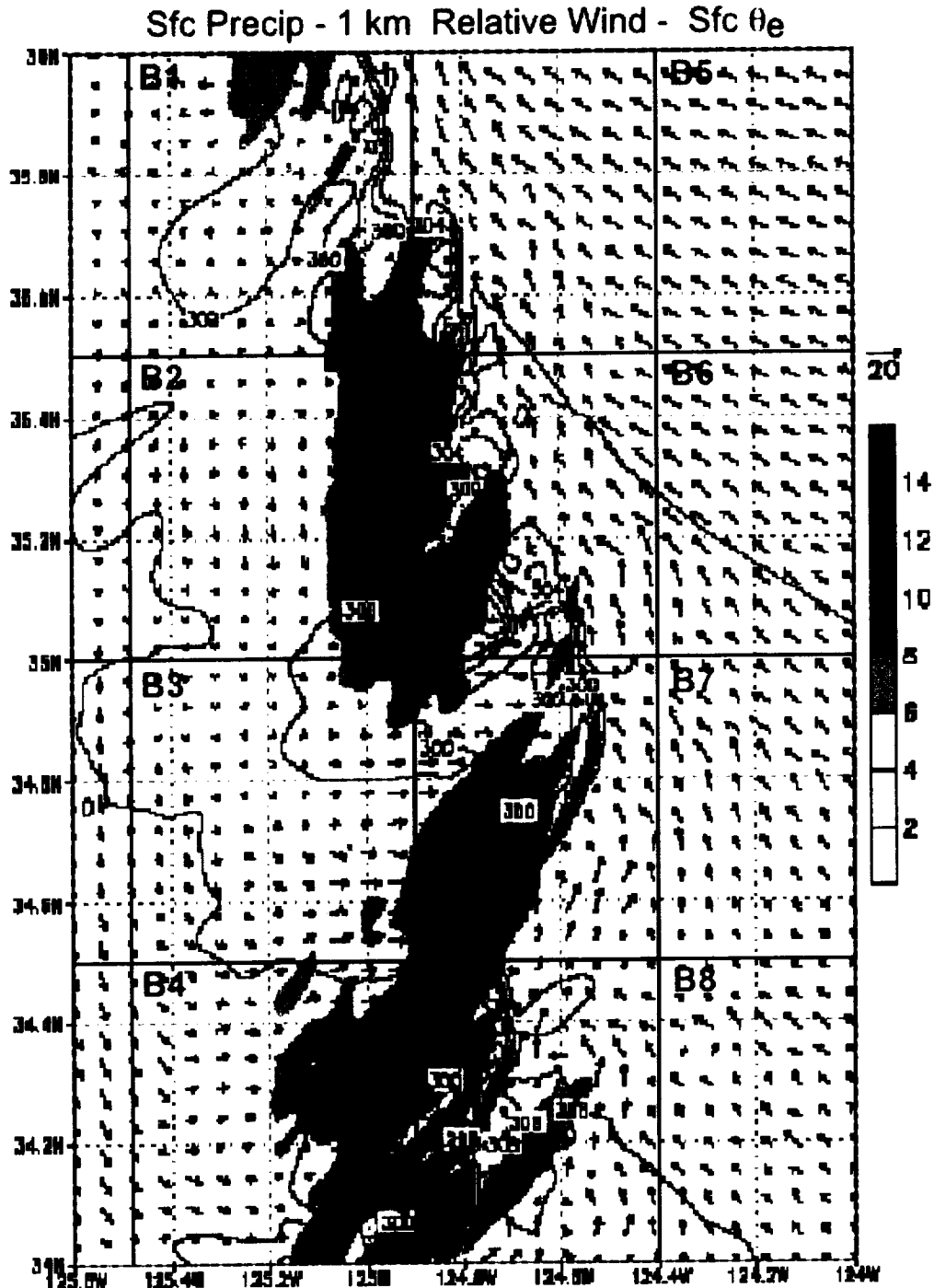


Fig. 18 Horizontal plot of model surface equivalent potential temperature (solid contours every 2 K) and system relative wind at 1 km MSL (system motion $u=12.8 \text{ m s}^{-1}$, $v=15.4 \text{ m s}^{-1}$) and surface precipitation (shaded contours mm h^{-1}) on the 1.3 km grid at 0600 UTC 19 February 2001. The color scale for the precipitation shading is shown to the right of the plot. The scaling vector for a 20 m s^{-1} vector is shown above the precipitation color scale. The boxes labeled B1 through B8 are averaging regions for vertical profiles shown in Fig. 19.

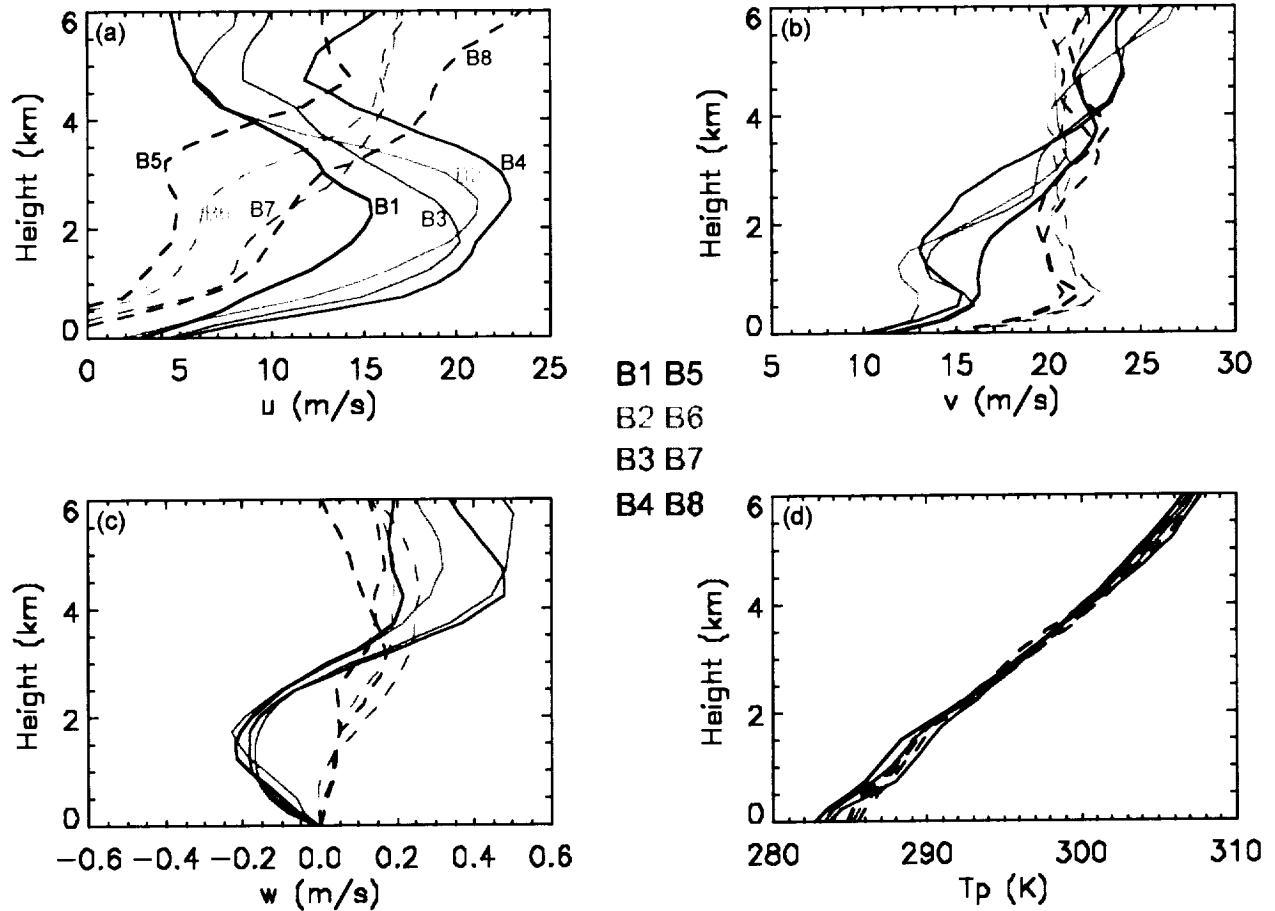


Fig. 19 Vertical profiles of (a) mean u (cross frontal) wind component (m s^{-1}), (b) mean v (along frontal) wind component (m s^{-1}), (c) mean vertical motion (m s^{-1}), and (d) equivalent potential temperature (K) for the regions shown in Fig. 18. Solid contours are for regions (B1 – B4) behind the NCFR while dashed contours are for regions (B5 – B8) ahead of the front.

P-3 Soundings 19 February

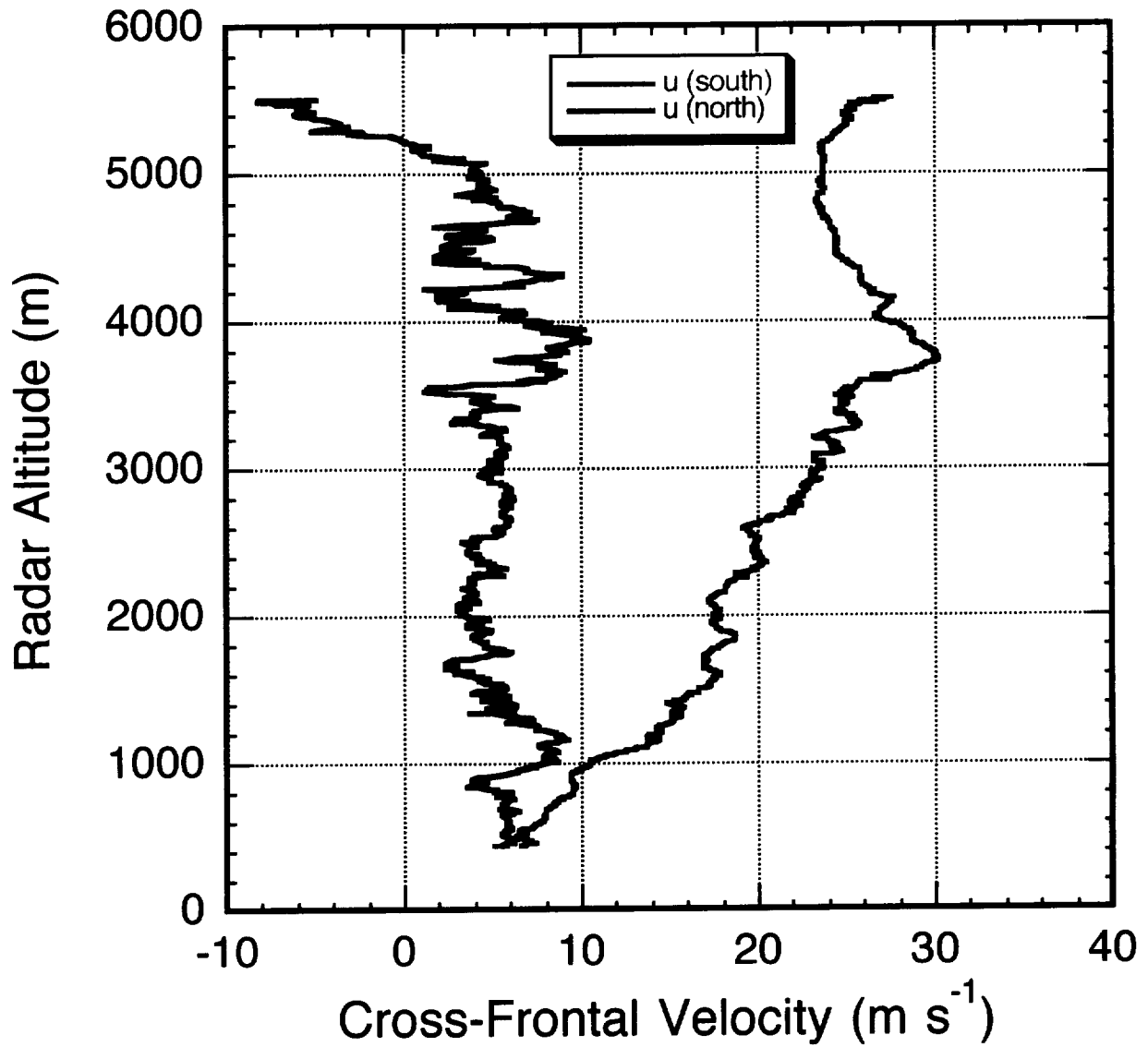


Fig. 20 Cross-frontal wind component (m s^{-1}) from the two P-3 ascent/descent soundings ahead of the NCFR shown in Fig. 6. The blue line is the northern most sounding, the red line the southernmost sounding.

MM5 Cross Section along 35.5N

Reflectivity (dBZ) and Vertical Velocity (cm s^{-1})

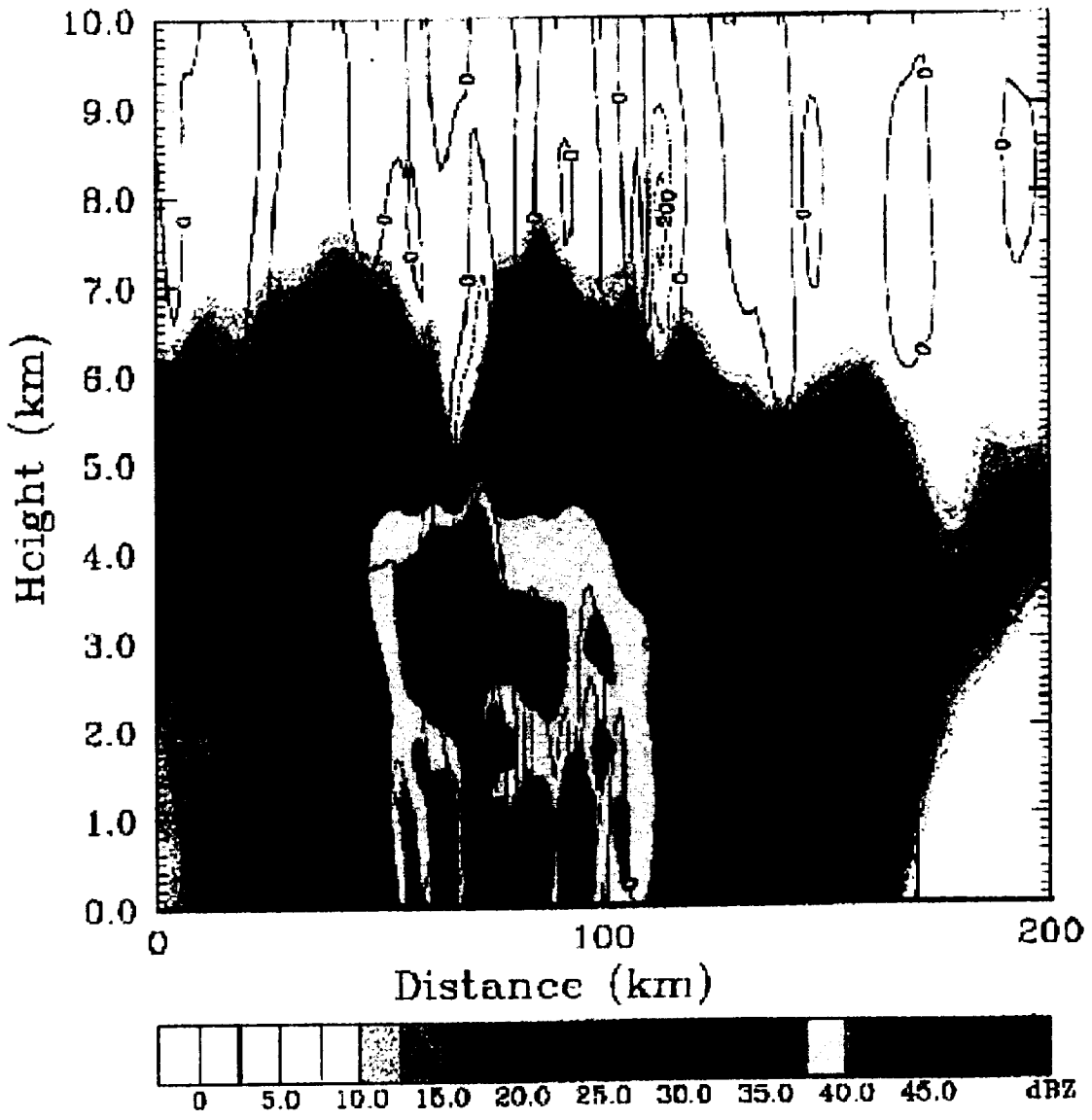


Fig. 21 Vertical cross section of model reflectivity (dBZ) and vertical velocity (cm s^{-1}) along an east-west line through the NCFR leading edge.

The Structure of a Pacific Narrow Cold Frontal Rainband

David P. Jorgensen
NOAA/National Severe Storm Laboratory

Zhaoxia Pu
Goddard Earth Sciences and Technology Center
University of Maryland, Baltimore County

Ola Persson
NOAA/ Environmental Technology Laboratory

Wei-Kuo Tao
NASA/Goddard Space Flight Center

Submitted to *Monthly Weather Review*

Popular Summary

Of the main types of extratropical-cyclone-related mesoscale rainbands, the most intense rainfall rates are usually associated with Narrow Cold Frontal Rainbands (NCFRs). A NOAA P-3 instrumented aircraft observed an intense, fast-moving NCFR as it approached the Pacific Northwest coast on 19 February 2001 during the Pacific Coastal Jets Experiment. The NCFR produced hail along the California coast when it made landfall. NCFRs are particularly hard to detect by coastal radars due to their shallow nature. The airborne Doppler radar found that the echo tops over the convective cores containing very high radar reflectivity, which characterized this NCFR at low levels, extended at altitudes extending only to ~4-5 km. An outstanding feature of this NCFR is the gaps (breaks) in the narrow band of high reflectivity, which is probably a result of hydrodynamic instability along the leading edge of the advancing cold pool.

This study used radar, dropsondes, in-situ data and mesoscale numerical simulations to document the detailed precipitation and kinematic structure of the NCFR. Specific attention was given to the structure of the gaps. Many aspects of NCFR structure seen in previous studies were confirmed. In addition, some new principal NCFR features were identified. In contrast to some earlier studies, density current theory described well the motion of the overall front. Based on radar analyses and numerical simulations, the updraft structure associated with heavy rainfall along the leading edge was shown to vary across the gap regions. The vertical shear of the cross-frontal low-level ambient flow exerted a strong influence on the updraft character. These new findings are consistent with theoretical arguments developed for squall lines describing the balance of vorticity at the leading edge, and also suggest that the mechanism for gap maintenance is not self-sustaining.